Ore Geology Reviews 101 (2018) 578–594

Contents lists available at ScienceDirect

Ore Geology Reviews

journal homepage: www.elsevier.com/locate/oregeorev

New constraints on the origin of the Maozu carbonate-hosted epigenetic Zn-Pb deposit in NE Yunnan Province, SW China

Lin-Jun Wang[a,c], Mei Mi[d], Jia-Xi Zhou[b,c,*], Kai Luo[c,e]

[a] Architecture Engineering College, Guizhou Minzu University, Guiyang 550025, China
[b] School of Resource Environment and Earth Sciences, Yunnan University, Kunming 650504, China
[c] State Key Laboratory of Ore Deposit Geochemistry, Institute of Geochemistry, Chinese Academy of Sciences, Guiyang 550081, China
[d] CAS Key Laboratory of Mineralogy and Metallogeny, Guangzhou Institute of Geochemistry, Chinese Academy of Sciences, Guangzhou 510640, China
[e] University of Chinese Academy of Sciences, Beijing 10049, China

ARTICLE INFO

Keywords:
NanoSIMS *in situ* S isotopes
LA-MC-ICPMS *in situ* Pb isotopes
Bulk Sr isotopes
Ore formation processes
The Upper Yangtze Zn-Pb metallogenic province, South China

ABSTRACT

Micro-scale isotopic compositions determined by micro-beam *in situ* analysis techniques are expected to provide new information for the understanding of ore genesis. Here we use the Maozu (~20 Mt of sulfide ore, grading 7.25 wt% Zn and 4.15 wt% Pb) Zn-Pb deposit in the Upper Yangtze Zn-Pb metallogenic province as a case study, utilizing NanoSIMS *in situ* S, femtosecond LA-MC-ICPMS *in situ* Pb and conventional bulk Sr isotopes, as well as field data, aimed to reveal its origin and ore formation process. NanoSIMS *in situ* $\delta^{34}S$ values of sulfide minerals from the Maozu deposit have a wider range (+5.9–+20.7‰) than that of bulk $\delta^{34}S$ values (+9.9–+19.9‰). Such S isotope signatures reflect the enrichment of heavy S isotopes in ore-forming fluids, and further indicate the source of S is multiple reservoirs (e.g. marine evaporites, coeval seawater, and metamorphic rocks/fluids). Pb isotopic ratios of galena determined by LA-MC-ICPMS *in situ* techniques have a narrower range ($^{206}Pb/^{204}Pb$ = 18.20–18.21, $^{207}Pb/^{204}Pb$ = 15.69–15.71 and $^{208}Pb/^{204}Pb$ = 38.40–38.43) than that of bulk Pb isotopic ratios ($^{206}Pb/^{204}Pb$ = 18.13–18.38, $^{207}Pb/^{204}Pb$ = 15.64–15.69 and $^{208}Pb/^{204}Pb$ = 38.22–38.58). This implies that *in situ* Pb isotopes can truly reflect the source of Pb, which is due to impurities enclosed by sulfide crystals and pollutants introduced by chemical analysis could significantly affect the quality of the bulk Pb isotopic data. Compared with previously reported Pb isotopic data of potential source rocks (i.e. late Permian Emeishan basalts, Paleozoic ore-bearing sedimentary rocks and Proterozoic basement metamorphic rocks), the *in situ* Pb isotopic data are significantly different from those of basalts, but are similar to those of both basements and sediments. This means that metal-rich fluids were mainly derived from and/or flowed through basements and sediments. Sphalerite separates have initial Sr isotopic ratios (0.711–0.719) that are distinctly different from those of ore formation age-corrected basalts ($^{87}Sr/^{86}Sr_{200\ Ma}$ = 0.704–0.708) and basements ($^{87}Sr/^{86}Sr_{200\ Ma}$ = 0.724–0.729), whereas partly overlap with those of age-corrected sediments ($^{87}Sr/^{86}Sr_{200\ Ma}$ = 0.707–0.714). Such Sr isotope signatures suggest that hydrothermal fluids were predominantly derived from and/or flowed through basements and sediments with a certain influence from basalts. Hence, the Maozu deposit has complex source rocks that are related to the local geological setting. The mixing of metal-rich fluids (related to basements and sediments, and even basalts) and S-bearing fluids (associated with multiple S reservoirs) plays a key role in the formation of sulfide ores. Therefore, the Maozu deposit, formed during Early Mesozoic (~196 Ma), is an epigenetic Zn-Pb deposit that hosts in carbonate rocks, occurs along fault-fold structures, and has a mixed source of mineralizing elements and associated fluids.

1. Introduction

The Maozu Zn-Pb deposit, located in the western margin of the Yangtze Block (Fig. 1a), is an important part of the Upper Yangtze Zn-Pb metallogenic province in South China (Fig. 1b; Zhou et al., 2018a). This province consists of > 400 carbonate-hosted Zn-Pb deposits (Liu and Lin, 1999; Zhou et al., 2013a; Wang et al., 2014) and accounts for 27% of total Zn + Pb resources in China (Zhang et al., 2015). In this province, several giant Zn-Pb deposits (> 1 Mt of Pb + Zn metal reserves) have been identified, including the world-class Huize (~30 Mt of sulfide ores, grading 25–35 wt% Zn + Pb: Zhou et al., 2001; Bao et al., 2017), Maoping (~25 Mt of sulfide ores with mean grades of

* Corresponding author at: School of Resource Environment and Earth Sciences, Yunnan University, Kunming 650504, China.
E-mail address: zhoujiaxi@ynu.edu.cn (J.-X. Zhou).

https://doi.org/10.1016/j.oregeorev.2018.08.012
Received 29 September 2017; Received in revised form 27 July 2018; Accepted 10 August 2018
Available online 11 August 2018
0169-1368/

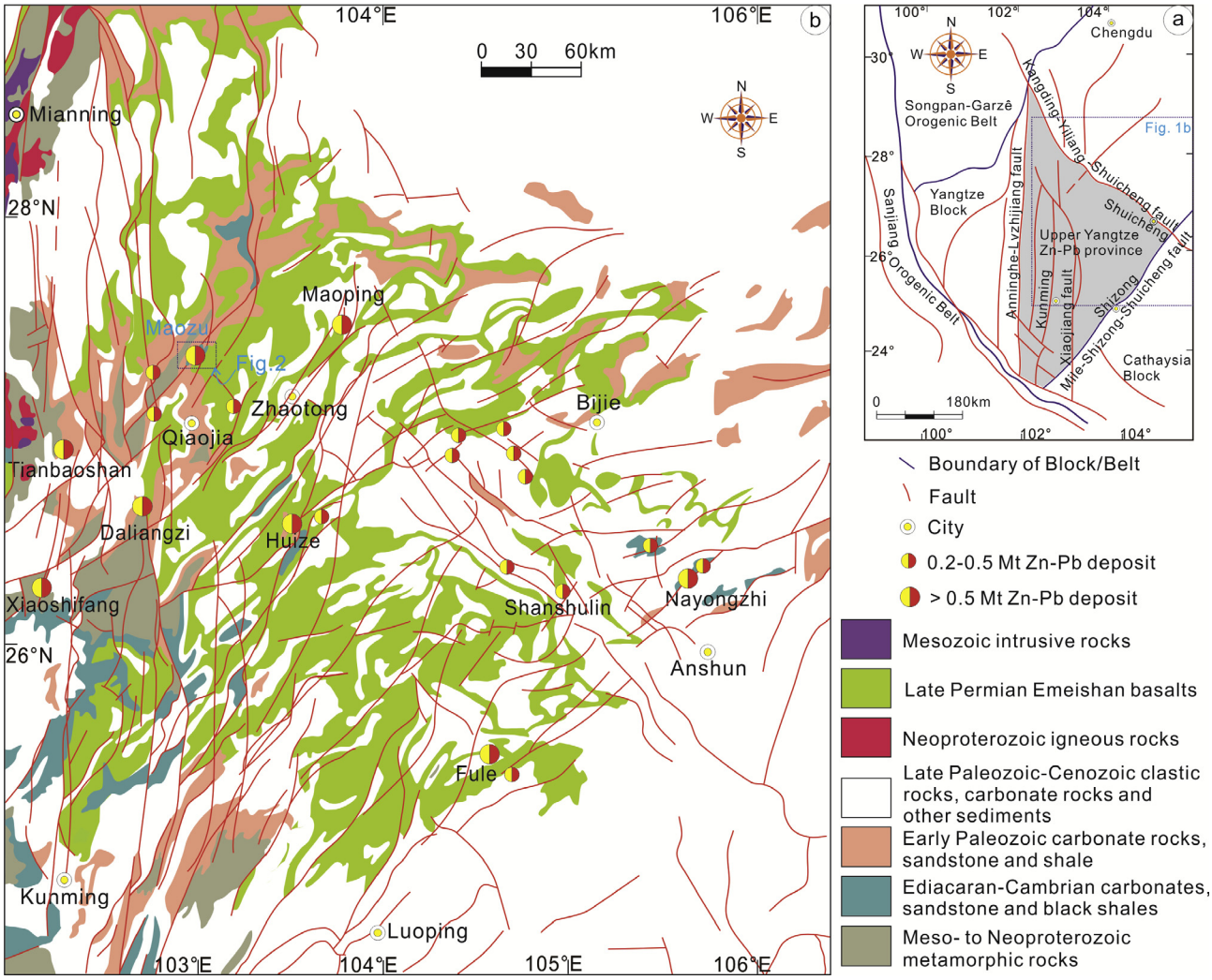

Fig. 1. a: Regional tectonic setting of the western Yangtze Block, highlighting the study area; b: Geological sketch map of the Upper Yangtze Zn-Pb metallogenic province (modified from Liu and Lin, 1999; Zhou et al., 2018a), showing the distribution of Zn-Pb deposits, faults, strata and igneous rocks.

15–35 wt% Zn + Pb: Wei et al., 2015), Daliangzi (~30 Mt of sulfide ores, grading 10–12 wt% Zn + Pb: Zheng and Wang, 1991), Tianbaoshan (~20 Mt of sulfide ores at mean grades of 10–15 wt% Zn + Pb: Zhou et al., 2013b; Sun et al., 2016), Maozu (~20 Mt of sulfide ores with mean grades of 7.25 wt% Zn and 4.15 wt% Pb: Zhou et al., 2013c) and Nayongzhi (~20 Mt of sulfide ores, grading 1.11–15.65 wt% Zn and 0.59–0.97 wt% Pb: Jin et al., 2016; Zhou et al., 2018b) Zn-Pb deposits. Among these deposits, the Maozu Zn-Pb deposit is characterized by: a) sulfide ores are structurally controlled by fault-fold tectonic systems and stratigraphically host in carbonate rocks of late Ediacaran (Figs. 1–3); b) sulfide ores have a spatially association with continental flood basalts of the Emeishan large igneous province (ELIP) (Figs. 1–3); c) sulfide ore bodies mainly occur in stratiform, veined or lentiform shape (Fig. 3b); and d) the ore-forming fluids having low-moderate temperatures (153–248 °C: Liu, 2009) and low salinities (2.8–5.3 wt% NaCl equiv.: He et al., 2006). Hence, some studies interpreted the Maozu Zn-Pb deposit as a type of sedimentary exhalative (SEDEX) or sedimentary reworking (e.g. Chen, 2002; He et al., 2006), whereas other researches considered it to be a Mississippi Valley-type (MVT) deposit (e.g. Liu, 2009; Jin et al., 2015). On the other hand, considering the Zn-Pb deposit and the ELIP exists a certain genetic relationship, there are also studies suggested that it may be a new unique SYG-type (e.g. Bao et al., 2013; Zhou et al., 2013c; Xu et al., 2014; Zheng et al., 2015). Such a new type of carbonate-hosted epigenetic Zn-Pb deposits is associated with igneous activities and occurs within compressional zones of passive margin tectonic setting (Zhou et al., 2018a,c), which are significantly different from those of typical MVT deposits (Leach et al., 2005, 2010). Therefore, the origin of the Maozu Zn-Pb deposit is still debated and its ore formation processes also need a more detailed investigation.

Sulfur (S) and lead (Pb) are two key ore-forming elements in Zn-Pb sulfide ore deposits, so their isotopes can be used to directly trace the sources of mineralizing elements and associated fluids (Ohmoto, 1972; Deloule et al., 1986; Kesler et al., 1994; Carr et al., 1995; Leach et al., 2005; Muchez et al., 2005; Anderson, 2008; Zhou et al., 2014a, 2016a). However, some crucial metallogenic information indicated from S and Pb isotopes is often masked by conventional whole-rock chemistry analysis, as impurities enclosed by sulfide crystals and/or pollutants introduced by chemical analysis could distinctly affect the quality of the determined data (Peevler et al., 2003; Ripley et al., 2010; LaFlamme et al., 2016; Jin et al., 2016; Bao et al., 2017; Tan et al., 2017; Zhou et al., 2018c). Such detailed information is crucial for the understanding of the formation of hydrothermal ore deposits. Micro-beam analysis techniques have been widely used to do *in situ* isotope analysis (Ikehata et al., 2008; Steinhoefel et al., 2009; Zhang et al., 2014; Yuan et al., 2015; Bao et al., 2016). Secondary ion mass spectroscopy (SIMS) and laser-ablation multi-collector inductively coupled plasma mass spectroscopy (LA-MC-ICPMS) are the two main equipment in the field

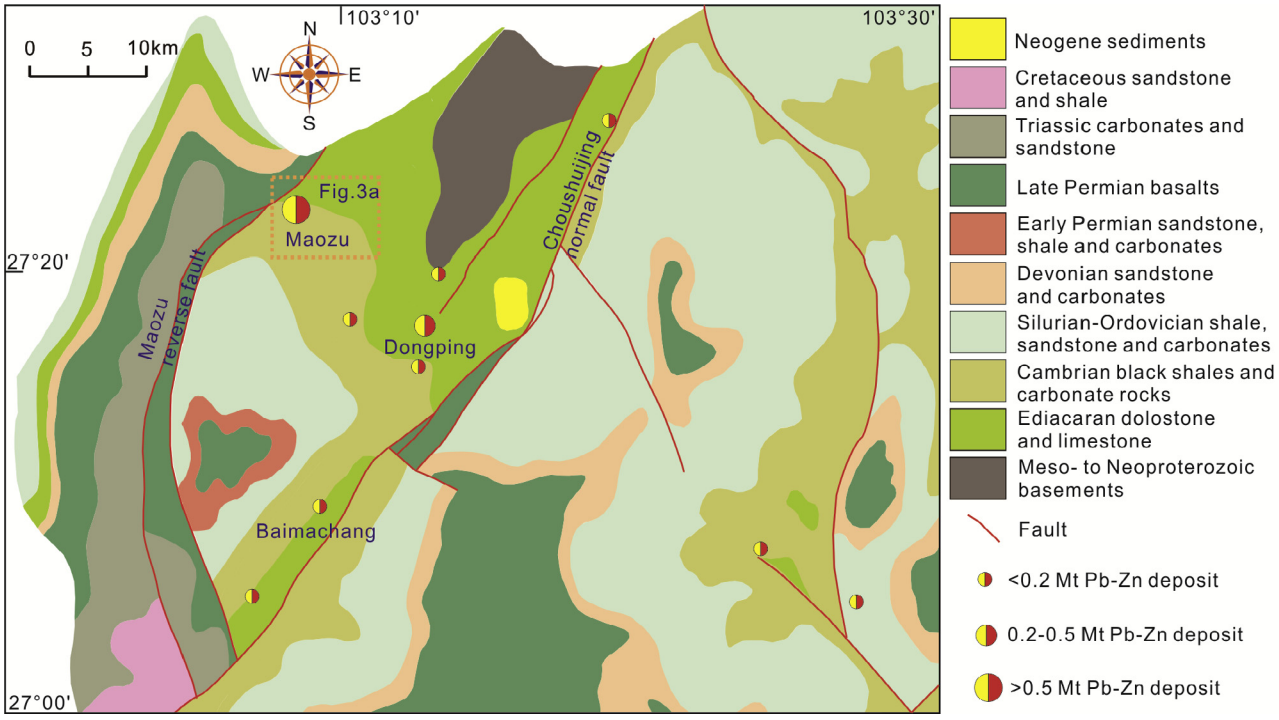

Fig. 2. Geological sketch map of the Maozu metallogenic district (modified from Liu and Lin, 1999), exhibiting the distribution of Zn-Pb deposits, strata, faults and basalts.

of micro-scale analysis (Li et al., 2010; Schmitt et al., 2010; Souders and Sylvester, 2010; Paul et al., 2011; Resano et al., 2013; Tang et al., 2014; Hauri et al., 2016).

Through integrated NanoSIMS *in situ* S, femtosecond LA-MC-ICPMS *in situ* Pb and conventional bulk Sr isotopic data, as well as detailed field data, this study aims to: a) trace the origin of mineralizing fluids; b) reveal the processes of Pb-Zn mineralization; c) determine the genetic relationship between Zn-Pb mineralization and the basalts of the ELIP; and d) built a new metallogenic model. These outcomes for understanding the formation of carbonate-hosted epigenetic Zn-Pb deposits and prospecting exploration have extensive significance.

2. Geology of the Maozu deposit

2.1. Regional geology

South China Block comprises of the Cathysia and Yangtze blocks, of which the latter is tectonically bounded by the Cathysia Block to south, the Sanjiang Orogenic Belt to the southwest and the Songpan-Ganzê Orogenic Belt to the northwest (Fig. 1a). The strata exposed in the western margin of the Yangtze Block consist of Proterozoic metamorphosed and folded basement complexes, and Paleozoic-Cenozoic cover sequences (Liu and Lin, 1999; Huang et al., 2004; Li et al., 2015; Zhou et al., 2014b, 2016b). The Proterozoic folded basements are composed of Meso- to Neoproterozoic metamorphic rocks that were later intruded by igneous rocks of Neoproterozoic and Mesozoic (Fig. 1b; Hu, 1999; Zhou et al., 2014c; Hu et al., 2017). The cover sequences are made up of sediments of Ediacaran-Triassic marine-facies and Jurassic-Quaternary continental facies (Zheng and Wang, 1991; Zhou et al., 2018a), and a few igneous rocks (mainly are the basalts of the ELIP) (Zhou et al., 2002). The marine sediments are mainly clastic rocks, carbonates and black shales, and are rich in gypsum-bearing evaporites and organic matters (Zhou et al. 2013d, 2018a; Liu et al., 2017a). Among these sedimentary rocks, platform carbonate sequences host > 400 Zn-Pb deposits, > 50% of which are hosted in carbonate rocks of late Ediacaran to early Cambrian (e.g. the Tianbaoshan, Maozu and Nayongzhi deposits: Zhou et al., 2013b,c, 2018b; Jin et al., 2016; Sun et al., 2016; Zhu et al., 2016) and Devonian to Carboniferous (e.g. the Maoping and Huize deposits: Wei et al., 2015; Bao et al., 2017). Structures are well-developed in the western Yangtze Block and have undergone Hercynian, Indosinian and Yanshanian orogenic events, and even Himalayan Orogeny (Qiu et al., 2016; Hu and Zhou, 2012; Hu et al., 2017; Zhou et al., 2018a). Sedimentation, magmatism and mineralization in the western margin of the Yangtze Block are strictly controlled by several regional deep-seated structures (Liu and Lin, 1999; Zhou et al., 2014c, 2018a), such as the Anninghe-Lvzhijiang and Xiaojiang faults (Fig. 1a).

A principal feature of the western Yangtze Block is the occurrence of the late Permian ELIP (~260 Ma) and its continental flood basalts, which covers an area of $\sim 0.7 \times 10^6$ km^2 (e.g. Zhou et al., 2002; Jian et al., 2009; Li et al., 2017; Liu et al., 2017b; Wang et al., 2018). Another principal feature of the western Yangtze Block is the occurrence of the Upper Yangtze Zn-Pb metallogenic province and its > 400 Zn-Pb sulfide ore deposits, which covers an area of $\sim 0.2 \times 10^6$ km^2 and have a spatially association with the flood basalts of the ELIP (e.g. Liu and Lin, 1999; Huang et al., 2010; Zhang et al., 2015; Zhou et al., 2018a). The Upper Yangtze Zn-Pb province is an important part of the giant South China low-temperature metallogenic domain (Hu et al., 2017) and has been the major source of base metals in China in the past several decades (Liu and Lin, 1999; Zhou et al., 2013a; Li et al., 2016).

After eruption of the ~260 Ma flood basalts of the ELIP, the Indosinian Orogeny (257–200 Ma) caused the closure of Paleotethys and the collision between the western margin of the Yangtze Block and the adjacent blocks (Reid et al., 2007; Hu and Zhou, 2012; Qiu et al., 2016). This event resulted in faulting and folding that controlled the distribution of carbonate-hosted epigenetic Zn-Pb deposits in the Upper Yangtze metallogenic province (e.g. Liu and Lin, 1999; Wang et al., 2014; Zhang et al., 2015; Zhou et al., 2018b). Timing of ore formation in the Upper Yangtze province is jointly constrained by model ages of Pb isotopes, and sphalerite/pyrite Rb-Sr, calcite/fluorite Sm-Nd and bitumen Re-Os isochron ages, which are between 245 and 192 Ma with a peaked age range of 230–200 Ma (e.g. Guan and Li, 1999; Li et al., 2007; Lin et al., 2010; Mao et al., 2012; Zhou et al., 2013a,c, 2015;

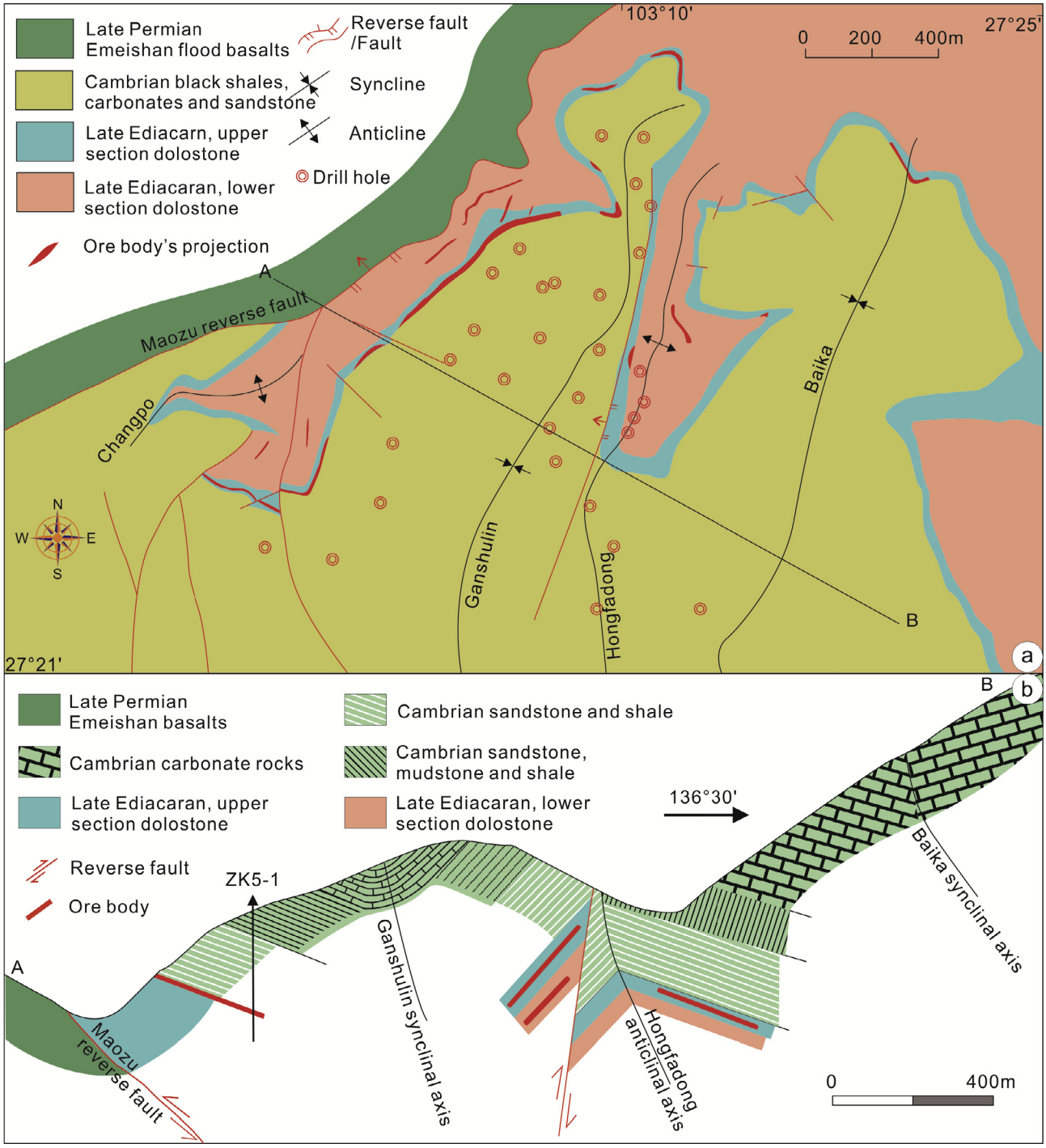

Fig. 3. a: Geological map of the Maozu Zn-Pb deposit (modified from Zhou et al., 2013c), displaying the distribution of Zn-Pb ore bodies, strata, faults, folds and basalts; b: A–B cross-section map of the Maozu deposit (modified from Zhou et al., 2013c), showing the occurrence of Zn-Pb ore bodies, strata, faults, folds and basalts.

Zhang et al., 2015; Hu et al., 2017). For example, Sm-Nd dating of hydrothermal calcite from the Maozu deposit yields an isochron age of 196 ± 13 Ma (Zhou et al., 2013c). This means that the Zn-Pb mineralization in the study region may be a response of the Indosinian Orogeny and the closure of Paleotethys.

2.2. Local geology

The Maozu deposit is located 48 km north Qiaojia City in NE Yunnan Province and is situated in the northwestern part of the Upper Yangtze province (Fig. 1b). The exposed strata in the Maozu region are Proterozoic, Ediacaran to Devonian, Permian to Triassic, Cretaceous and Neogene (Fig. 2). The Proterozoic strata are Meso- to Neoproterozoic Kunyang Group, which is composed of low-grade metamorphic rocks, such as phyllite and sandstone (Liu and Lin, 1999). These rocks are unconformably overlain by the late Ediacaran Dengying Formation that mainly consists of carbonate rocks. In turn, the Dengying Formation carbonate rocks are overlain by Cambrian strata that dominantly comprise of carbonate rocks, sandstone and black shales. These sedimentary rocks of Ediacaran and Cambrian are overlain by Silurian-

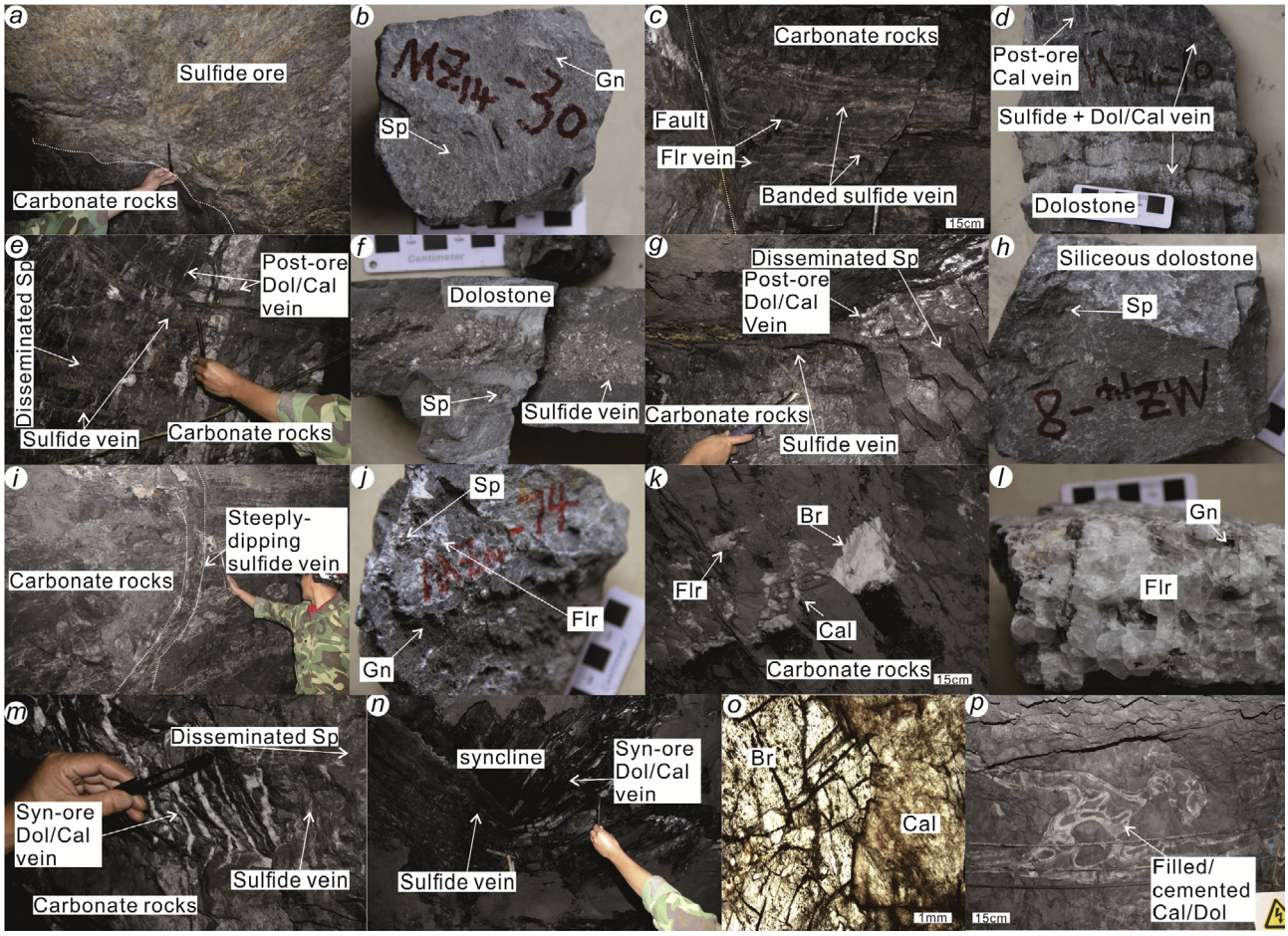

Fig. 4. Photographs display the main features of sulfide ores, gangue minerals, faults and wall rocks. a: Massive sulfide ore and its boundary with carbonate rocks; b: Massive sulfide ore, sphalerite (Sp) and galena (Gn) form densely massive aggregate; c: Fluorite (Flr) veins and banded sulfide veins occur along fractures within carbonate rocks, which are dislocated by reverse fault; d: Banded ore, sulfide and dolomite/calcite (Dol/Cal) form banded veins within dolostone, which are inserted by post-ore Cal veins; e: Sulfide veins present along fractures within carbonate rocks and disseminated Sp in wall rocks, as well as post-ore Dol/Cal veins crosscut sulfide veins; f: Veined ore, sulfide vein and disseminated Sp within dolostone; g: Disseminated Sp and sulfide veins in carbonate rocks and post-ore Dol/Cal veins filled fractures within carbonate rocks; h: Disseminated ore, disseminated Sp in siliceous dolostone; i: Steeply-dipping sulfide vein occurs along dip fault within carbonate rocks; j: Sp and Gn form densely massive aggregate, which is filled by Flr vein; k: Post-ore hydrothermal Flr, Cal and barite (Br) within carbonate rocks; l: Gn enclosed by Flr; m: Syn-ore Dol/Cal veins and sulfide veins, as well as disseminated Sp within carbonate rocks; n: Syn-ore Dol/Cal veins and sulfide veins within syncline; o: Br coexists with Cal; p: Post-ore Dol/Cal vein fills or cements salt-collapse structure.

Ordovician strata that predominantly consist of sandstone, shale and carbonate rocks. Silurian-Ordovician sedimentary rocks are overlain by sandstone and carbonate rocks of Devonian, which are in turn unconformably overlain by early Permian strata that mainly consist of sandstone, shale and carbonate rocks (Zhou et al., 2013c). Early Permian sedimentary rocks are unconformably overlain by late Permian basalts of the ELIP, which are in turn unconformably overlain by Triassic sedimentary rocks. The Triassic rocks are unconformably overlain by Cretaceous strata that are dominantly composed of sandstone and shale. The sporadically distributed Neogene strata in this region are made up of continental sediments (Fig. 2).

Structures are mainly the Maozu reverse fault and Choushuijing normal fault (Fig. 2), as well as several folds (Fig. 3a). The flood basalts of the ELIP are the only igneous rocks in this region (Fig. 2). About 10 carbonate-hosted Zn-Pb deposits have been discovered until now (Fig. 2), such as the Maozu, Dongping and Baimachang deposits, of which the Maozu deposit that contains ~20 Mt of sulfide ores with mean grades of > 10 wt% Pb + Zn is the largest one.

Zhou et al. (2013c) has extensively described the geology of the Maozu ore deposit, therefore only a brief account of the local geology is given here. In the Maozu mining area, the exposed strata include Ediacaran, Cambrian and Permian (Fig. 3a and b). The late Ediacaran Dengying Formation mainly consists of dolostone and limestone, which are conformably overlain by dolostone, limestone, sandstone and black shales of Cambrian. The basalts of late Permian unconformably overlie sedimentary rocks of Cambrian and Ediacaran Dengying Formation. In the Maozu mining area, the Maozu reverse fault is the most important ore-controlling fault structure, which trends NE in the north part, but NW in the south part, with > 30 km long (Figs. 2 and 3). The Dengying Formation and Cambrian sedimentary rocks formed the Ganshulin and Baika synclines, and Hongfadong and Changpo anticlines (Fig. 3a and b). The axial trend of the Ganshulin, Baika and Hongfadong fold structures is N20°E, whereas the Changpo anticline trends N40°E.

2.3. Mineralization

Sulfide ore bodies in the Maozu mining area are lithologically hosted in the Dengying Formation dolostone and structurally occur within a kilometer-scale fault-fold tectonic system (Fig. 3a). Four stratiform or lentiform ore bodies have been identified in the upper section of the Dengying Formation, which are 440–850 m long, 221–725 m wide and 2.63–5.09 m thick, grading 0.77–6.11 wt% Pb and 3.85–11.48 wt% Zn. The Zn/Pb ratios have a range from 5 to 9. Five stratiform or lentiform ore bodies have been recognized in the lower

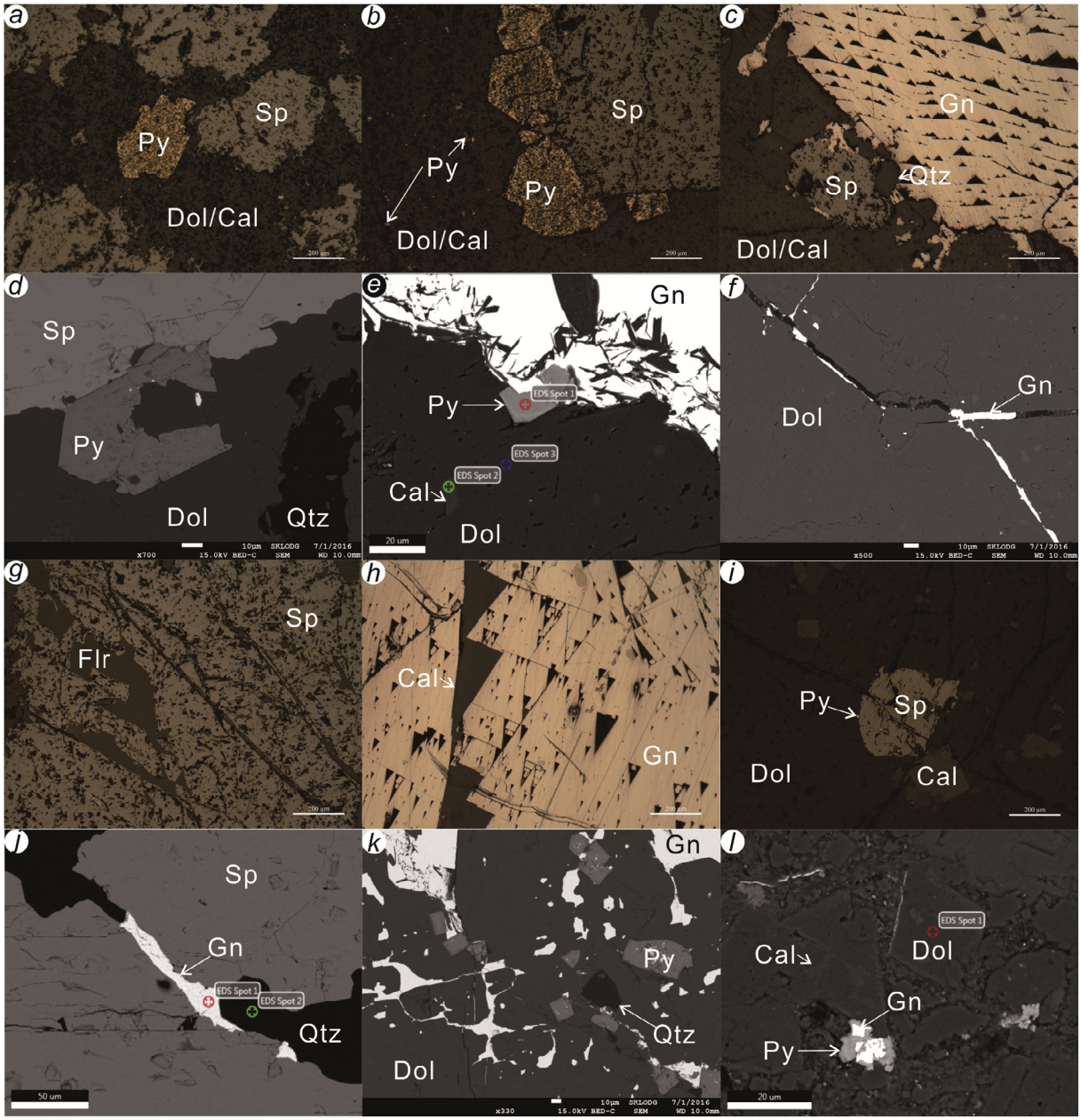

Fig. 5. Main textural features of hydrothermal minerals under microscope and scanning electron microscope (SEM). a: Granular pyrite (Py) coexists with fine- to medium-grained sphalerite (Sp), both of which are cemented by dolomite/calcite (Dol/Cal); b: Fine-grained Py is cemented by Dol/Cal, which coexists with medium granular Py and Sp; c: Coarse-grained Gn coexists with fine-grained Sp and quartz (Qtz), as well as Dol/Cal, of which Gn shows stress deformation texture; d: Coarse granular Sp coexists with Py, Dol and Qtz; e: Coarse-grained Gn coexists with fine-grained Py and coarse granular Dol that forms solid-solution texture with Cal; f: Veined Gn fills into fracture within Dol; g: Fluorite (Flr) vein fills into fracture within Sp; h: Coarse granular Gn has stress deformation texture and is filled by Cal vein; i: Granular Sp, Py and Cal are cemented by Dol; j: Veined Gn and Qtz fill into fracture within Sp; k: Fine granular Py, Qtz and Gn are enclosed by Dol that coexists with medium-grained Gn, and is cemented by veined Gn; l: Fine granular Py and Gn are enclosed by Dol that contains Cal solid-solution.

section of the Dengying Formation, which are 240–930 m long, 45–346 m wide and 1.73–8.29 m thick, with grades of 1.13–7.2 wt% Pb and 3.61–12.27 wt% Zn. The Zn/Pb ratios have a range of 3–5. Ore bodies in the two sections are occurred along bedding-plane structures within the Dengying Formation (Fig. 3b). In addition, two veined ore bodies occur within steeply-dipping fault zone (Fig. 4i and j), which are 60–94 m in length, 47–80 m in width and 4.04–5.96 m in thickness, grading 1.36–4.4 wt% Pb and 5.24–8.36 wt% Zn. Ore bodies of this type trend dominantly N20-43° W. The total Pb + Zn sulfide ore reserves are ~20 Mt with average grades of 4.15 wt% Pb and 7.25 wt% Zn (Liu, 2009). In addition, this deposit also contains abundant elements of Ag, and Ga, Cd and Ge, which host dominantly in galena and sphalerite, respectively (Liu, 2009; Zhou et al., 2013c; Zheng et al., 2015).

Sulfide ores in stratiform, lentiform and veined ore bodies are made up mainly of sphalerite, galena, and pyrite as ore minerals, and calcite, dolomite, quartz, fluorite and barite as gangue minerals (Figs. 4 and 5). Sulfide ores occur as either massive (Fig. 4a and b), banded (Fig. 4c and d), veined (Fig. 4e and f) or disseminated (Fig. 4e, g and h and m) structure. The veined and disseminated sulfide ores generally occur surrounding the massive and banded ones in space (Fig. 4a and h). In massive ore, sulfide minerals are densely distributed (Fig. 4b); in banded ore, ore sulfides and gangue minerals form inter-bedded veins (Fig. 4d); in veined ore, sulfides form centimeter-scale veins and occur in fracture within dolostone (Fig. 4m and n); and in disseminated ore,

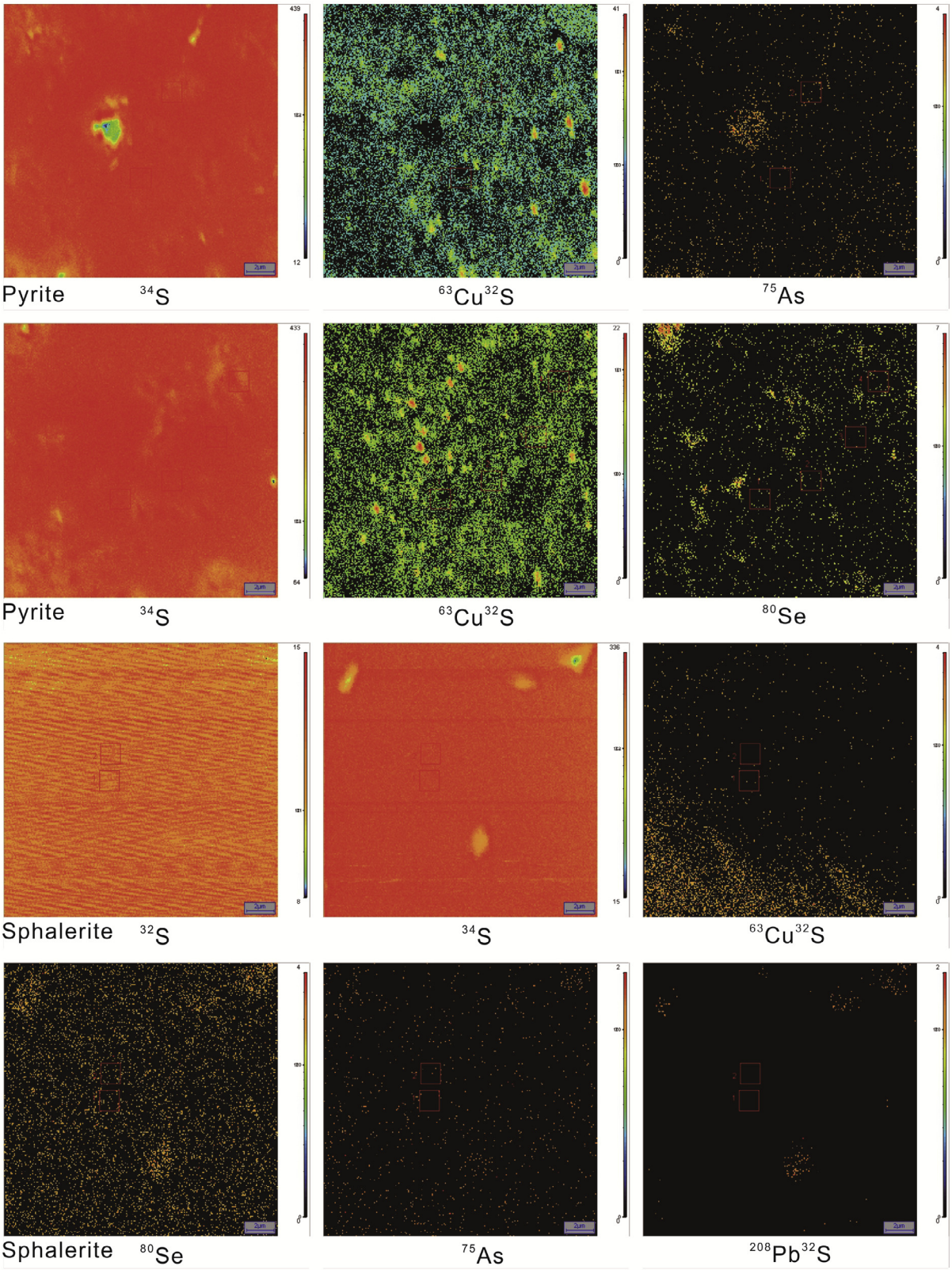

Fig. 6. The selected area in pyrite and sphalerite for *in situ* S isotope analysis with homogeneous isotopic compositions (such as ^{32}S, ^{34}S, ^{75}As and $^{63}Cu^{32}S$ mapping).

sulfides occur as single crystal or speckle aggregate that has star-like distribution in dolostone (Fig. 4h and l). Most hydrothermal minerals have granular (Fig. 5a, b and i), embayment (Fig. 5c, d), filled (Fig. 5e–g and f), enclosed (Fig. 5h, i), solid-solution (Fig. 5e, i and l) or stress deformation (Fig. 5c and h) texture. For example, sphalerite is fine- to medium-grained and coexists with granular pyrite (Fig. 5a) or galena (Fig. 5c), as well as is enclosed by calcite/dolomite (Fig. 5i) or is filled by fluorite (Fig. 5g), galena or quartz (Fig. 5j); granular pyrite is

Table 1
In situ and bulk S isotopic compositions of sulfides from the Maozu deposit.

No.	Structure	Mineral	$\delta^{34}S$/‰	Source	No.	Mineral	$\delta^{34}S$/‰	Source
MZ_{14}-21-1	Banded ores	Sphalerite	+16.2	This paper; NanoSIMS *in situ*	Mao-11	Sphalerite	+13.9	Liu and Lin (1999)
MZ_{14}-21-2		Sphalerite	+17.0		Mao-8-2	Sphalerite	+11.5	
MZ_{14}-21-3		Sphalerite	+17.0		Mao-8-2	Galena	+8.8	
MZ_{14}-21-4		Sphalerite	+17.1		Mao-3	Pyrite	+19.9	
MZ_{14}-21-5		Pyrite	+5.9		Mao-2	Barite	+30.4	
MZ_{14}-21-6		Pyrite	+6.2		M-1	Sphalerite	+10.7	Liu (2009)
MZ_{14}-30-1	Massive ores	Sphalerite	+15.9		M-2	Galena	+11.9	
MZ_{14}-30-2		Pyrite	+11.2		MZ-5	Sphalerite	+13.4	Zhou et al. (2013c)
MZ_{14}-44-1	Massive ores	Sphalerite	+8.4		MZ-11	Sphalerite	+13.5	
MZ_{14}-44-2		Sphalerite	+9.6		MZ-40	Galena	+9.9	
MZ_{14}-58-1	Veined ores	Pyrite	+14.6		MZ-21	Galena	+15.4	
MZ_{14}-58-2		Pyrite	+17.8		MZ-36	Galena	+13.9	
MZ_{14}-77-1	Disseminated ores	Pyrite	+20.7		MZ-38	Galena	+19.2	
MZ_{14}-77-2		Sphalerite	+16.3		MZ-34	Galena	+12.1	
MZ_{14}-77-3		Pyrite	+19.2		MZ-37	Galena	+14.2	

enclosed and filled by calcite/dolomite (Fig. 5a and l); granular galena has stress deformation texture (Fig. 6e and h); eutectic sphalerite and galena form embayment texture (Fig. 5c); and calcite and dolomite usually form solid-solution texture (Fig. 5e, i and l). These hydrothermal minerals formed during sulfide ± calcite/dolomite ± quartz ± fluorite (Figs. 4 and 5) and calcite/dolomite ± quartz ± fluorite ± barite (Fig. 4k and o) two mineralization phases.

2.4. Wall rock alteration

Wall rock alteration such as carbonatization (dolomite ± calcite), silicification (quartz), fluoritization (fluorite) and baratization (barite) is well-developed in the Maozu mining area. Carbonatization formed coarse-granular recrystallized dolostone (Fig. 4a), or dolomite/calcite cements (Fig. 4d, g and o, p); silicification generated silicified dolostone (Fig. 4h) or quartz cements (Fig. 5j); fluoritization occurred as fluorite cements (Fig. 4j) or fragments (Fig. 4l); and baratization formed barite fragments (Fig. 4k). Among these altered minerals, the dolomite/calcite, quartz and fluorite are often spatially associated with Zn and Pb sulfide minerals and are important ore prospecting clues.

3. Samples and analytical methods

3.1. Samples

Hand specimens of sulfide ores were sampled from the main stratiform Zn-Pb ore bodies in the Maozu ore district through underground mining tunnels. These samples have a variety of structures, including massive, banded, veined and disseminated ores (Tables 1–3). On the basis of microscope observation and scanning electron microscopy (SEM) analysis, ten polished thin sections (main ore formation stage) were selected for micro-scale *in situ* S (NanoSIMS) and Pb (LA-MC-ICPMS) isotope analyses. In addition, three sphalerite separates were handpicked from three samples of sulfide ores (main stage) under binocular for Rb-Sr (TIMS) isotope analyses. Pyrite and sphalerite were selected for NanoSIMS *in situ* S isotope analysis, due to those two sulfide minerals have standard samples. In addition, the *in situ* Pb isotopic ratios of pyrite and sphalerite were not determined by LA-MC-ICPMS, because of the high Hg contents within them that could dramatically affect the quality of the obtained data (Bao et al., 2016, 2017; Tan et al., 2017).

3.2. Analytical methods

3.2.1. In situ S isotope analysis

In situ S isotopic compositions were determined using a CAMECA NanoSIMS at the Key Laboratory of Earth and Planetary Physics, Institute of Geology and Geophysics, Chinese Academy of Sciences. This instrument has three different settings for Faraday cups/electron multiplier detectors to meet the diverse requirements of spatial resolution. The standard-sample-standard bracketing method was used to calibrate the instrumental mass fractionation. Target spots of homogeneous isotopes (such as ^{32}S, ^{34}S and ^{75}As in Fig. 6) within sulfide crystals were selected for micro-scale S isotope analysis in order to obtain the credible data. International standards included Balmat (pyrite and sphalerite) and CAR-123 (pyrite), and internal standards included PY-1117 (pyrite), CS-01 (pyrite), JC-14 (sphalerite) and MY09-12 (sphalerite). The analytical error was 0.2‰ (1σ). Details of NanoSIMS instrument parameters and S isotope analysis were available in Zhang et al. (2014) and Zhou et al. (2018b).

3.2.2. In situ Pb isotope analysis

In situ Pb isotope analysis was performed using a Nu II MC-ICPMS combined with a 266 nm femtosecond laser ablation system at the State Key Laboratory of Continental Dynamics, Northwest University. The polished thin sections needed to clean with milli-Q water (18.2 MΩ·cm) before Pb isotope analysis. Laser ablation was made of 20 s background collection followed by 50 s signal collection. Spot size of laser ablation is 15 μm. 100% output energy: > 600 μJ; 100% energy density: 6 J/cm^2; laser frequency: 5–50 Hz; and ablation way: line 3 μm/s. The Tl (20 ppb, NIST SRM 997, $^{205}Tl/^{203}Tl = 2.38890$) and NIST SRM 610 glass were served as internal and external standards, respectively. The repeated analysis of NIST SRM 610 glass standard yielded highly reliable and reproducible results during the whole analytical process with mean $^{206}Pb/^{204}Pb$, $^{207}Pb/^{204}Pb$ and $^{208}Pb/^{204}Pb$ ratios of 17.052 ± 0.003, 15.515 ± 0.003 and 36.980 ± 0.007 (1 s, $n = 183$), respectively. Details of LA-MC-ICPMS instrument parameters and Pb isotope analysis were available in Bao et al. (2016) and Zhou et al. (2018c).

3.2.3. Rb-Sr isotope analyses

Rb-Sr isotope analyses were completed using GV Isoprobe-T thermal ionization mass spectrometer (TIMS) at the Beijing Research Institute of Uranium Geology. The separation and purification of Rb and Sr from matrix elements were accomplished using Spec-Sr ion exchange resin. The procedure blank is 6 pg (10^{-12} g) for Rb and 5 pg for Sr. The mass fractionation was calibrated using an $^{88}Sr/^{86}Sr$ ratio of 8.37521. The repeated analysis of NBS 987 standard yielded highly reliable and reproducible results with a mean $^{87}Sr/^{86}Sr$ ratio of 0.710244 ± 5 (2σ, $n = 15$). The uncertainty (2σ) is 0.005% for $^{87}Sr/^{86}Sr$ and 2% for $^{87}Rb/^{86}Sr$. Details of Rb-Sr isotope analyses were available in Li et al. (2005) and Zhou et al. (2013a).

Table 2
In situ and bulk Pb isotopic ratios of sulfides from the Maozu deposit.

No.	Structure	Mineral	$^{206}Pb/^{204}Pb$	1s	$^{207}Pb/^{204}Pb$	1s	$^{208}Pb/^{204}Pb$	1s	$^{208}Pb/^{206}Pb$	1s	$^{207}Pb/^{206}Pb$	1s	Source
MZ_{14}-21-01	Banded ores	Galena	18.202	0.002	15.699	0.002	38.412	0.006	2.1101	0.0001	0.86242	0.00002	This paper; Fs LA-MC-ICPMS
MZ_{14}-21-02			18.204	0.002	15.701	0.002	38.422	0.007	2.1104	0.0001	0.86249	0.00003	
MZ_{14}-21-03			18.207	0.002	15.705	0.002	38.432	0.006	2.1107	0.0001	0.86255	0.00002	
MZ_{14}-25-01	Massive ores		18.203	0.002	15.700	0.002	38.419	0.005	2.1105	0.0001	0.86247	0.00002	
MZ_{14}-25-02			18.208	0.002	15.704	0.002	38.430	0.005	2.1106	0.0001	0.86249	0.00002	
MZ_{14}-25-03			18.205	0.002	15.701	0.002	38.421	0.005	2.1103	0.0001	0.86246	0.00002	
MZ_{14}-25-04			18.205	0.002	15.699	0.002	38.402	0.006	2.1097	0.0001	0.86234	0.00003	
MZ_{14}-42-01	Veined ores		18.199	0.002	15.691	0.002	38.399	0.006	2.1098	0.0001	0.86231	0.00003	
MZ_{14}-42-02			18.199	0.002	15.693	0.002	38.399	0.006	2.1097	0.0001	0.86233	0.00002	
MZ_{14}-42-03			18.202	0.002	15.696	0.002	38.403	0.006	2.1097	0.0001	0.86232	0.00002	
MZ_{14}-42-04			18.209	0.002	15.707	0.002	38.431	0.006	2.1104	0.0001	0.86249	0.00002	
MZ_{14}-60-01	Disseminated ores		18.205	0.002	15.701	0.003	38.416	0.007	2.1101	0.0001	0.86244	0.00003	
MZ_{14}-60-02			18.207	0.002	15.703	0.002	38.424	0.006	2.1102	0.0001	0.86244	0.00002	
MZ_{14}-60-03			18.208	0.002	15.705	0.002	38.424	0.006	2.1101	0.0001	0.86246	0.00002	

No.	Mineral	$^{206}Pb/^{204}Pb$	2s	$^{207}Pb/^{204}Pb$	2s	$^{208}Pb/^{204}Pb$	2s	$^{208}Pb/^{206}Pb$	$^{207}Pb/^{206}Pb$	Source
MZ-11	Sphalerite	18.375	0.003	15.686	0.003	38.577	0.006	2.0994	0.85366	Zhou et al. (2013c)
MZ-5	Sphalerite	18.260	0.001	15.655	0.001	38.396	0.002	2.1027	0.85734	
MZ-21	Sphalerite	18.161	0.002	15.640	0.002	38.246	0.004	2.1059	0.86119	
MZ-34	Galena	18.162	0.005	15.644	0.004	38.272	0.009	2.1073	0.86136	
MZ-40	Galena	18.194	0.004	15.676	0.002	38.362	0.006	2.1085	0.86160	
MZ-36	Galena	18.129	0.002	15.658	0.001	38.220	0.003	2.1082	0.86370	
MZ-21	Galena	18.170	0.002	15.660	0.002	38.313	0.004	2.1086	0.86186	

4. Analytical results

4.1. *In situ* $\delta^{34}S$ values

In situ and previously reported bulk $\delta^{34}S$ values are listed in Table 1 and are shown in Figs. 7 and 8. Sulfide crystals have NanoSIMS *in situ* $\delta^{34}S$ values ranging from +5.9 to +20.7‰ (mean +14.2‰), of which pyrite crystals have $\delta^{34}S$ values ranging from +5.9 to +20.7‰ (average +13.7‰), and $\delta^{34}S$ values of sphalerite range from +8.4 to +17.1‰ (average +14.7‰) (Fig. 7). It is clear that there is no significant difference in the *in situ* $\delta^{34}S$ values between pyrite and sphalerite crystals. In addition, there is no significant difference of sulfur isotopic compositions among different types of ores (Table 1). On the other hand, compared with bulk $\delta^{34}S$ values of sulfides (+8.8–+19.9‰, mean +13.45‰; Liu and Lin, 1999; Liu, 2009; Zhou et al., 2013c), *in situ* S isotopic data have a much wider range (Fig. 8a and b).

4.2. *In situ* Pb isotopic ratios

In situ and previously reported bulk Pb isotopic ratios are presented in Table 2 and are shown in Figs. 9 and 10. Galena crystals have LA-MC-ICPMS *in situ* $^{206}Pb/^{204}Pb$, $^{207}Pb/^{204}Pb$, and $^{208}Pb/^{204}Pb$ ratios ranging from 18.20 to 18.21, 15.69 to 15.71, and 38.40 to 38.43, respectively. It is clear that there is no obvious difference of Pb isotopic ratios among different types of ores (Table 2). Compared with bulk Pb isotopic data ($^{206}Pb/^{204}Pb$ = 18.13–18.38, $^{207}Pb/^{204}Pb$ = 15.64–15.69, and $^{208}Pb/^{204}Pb$ = 38.22–38.58; Zhou et al., 2013c), *in situ* Pb isotopic data have a much narrower range (Figs. 9 and 10).

4.3. Rb-Sr isotopic ratios

This study and previously reported Rb-Sr isotopic ratios are listed in Table 3 and are shown in Fig. 11. Sphalerite separates have very low concentrations of Rb (0.075–0.103 × 10^{-6}) and relatively low Sr contents (0.313–3.14 × 10^{-6}). $^{87}Rb/^{86}Sr$ and $^{87}Sr/^{86}Sr$ ratios of sphalerite separates range from 0.095 to 0.833 and 0.712634 to 0.714869, respectively. There is no obvious change trend of Sr isotopic ratios among different types of ores (Table 3). Although influenced by some factors, sphalerite Rb-Sr isotope system did not yield ideal isochron age, previous Sm-Nd dating of hydrothermal calcite suggested that the Maozu deposit was likely formed at ~200 Ma (Zhou et al., 2013c). Therefore, using this age to correct the initial Sr isotopes, we obtain the $^{87}Sr/^{86}Sr_{200\ Ma}$ ratios of all sphalerite separates, which have a range from 0.711 to 0.719 (Fig. 11). Such initial Sr isotope signatures indicate that sphalerite is rich in radiogenic Sr isotopes.

5. Discussion

5.1. Source of reduced S and its formation mechanism

5.1.1. A single S source or multiple S reservoirs?

It is well-known that the $\delta^{34}S$ values of S-bearing minerals in hydrothermal systems are mainly depending on their sources and fractionation (Ohmoto and Goldhaber, 1997; Hoefs, 2015; Seal et al., 2000; Rye, 2005; Sharp, 2017). Previous studies of S isotopes in sulfide and sulfate minerals suggested that S in MVT deposits can be derived from various sources, including evaporites, H_2S reservoir gas, connate seawater, organically bound S, diagenetic pyrite, and even mantle- or metamorphism-derived S (Jones et al., 1996; Chi and Savard, 1997; Leach et al., 2010; Bai et al., 2013; Zhou et al., 2013d, 2018a; Zhu et al., 2016). Among these sources, mantle-derived S has $\delta^{34}S$ values ranging from −3 to +3‰ (Chaussidon et al., 1989); $\delta^{34}S$ values of igneous rocks range from −5 to +15‰ (Ohmoto, 1972; Seal et al., 2000); metamorphic rocks/fluids have $\delta^{34}S$ values ranging from −20 to +20‰ (Ohmoto, 1986; Seal, 2006); ancient (Cambrian-Permian)

Table 3
Bulk Rb-Sr isotopic ratios of sulfides from the Maozu deposit.

No.	Structure	Mineral	$Rb/10^{-6}$	$Sr/10^{-6}$	$^{87}Rb/^{86}Sr$	$^{87}Sr/^{86}Sr$	2σ	$^{87}Sr/^{86}Sr_{200\ Ma}$	Source
MZ-5		Sphalerite	0.05	0.33	0.4704	0.718700	0.000017	0.71745	Zheng et al. (2015)
MZ-18		Sphalerite	0.06	2.86	0.0588	0.710785	0.000013	0.71061	
MZ-21		Sphalerite	0.1	0.36	0.8497	0.720965	0.000012	0.71868	
MZ-34		Sphalerite	0.06	0.92	0.1834	0.716921	0.000010	0.71638	
MZ-37		Sphalerite	0.18	10.02	0.0519	0.711738	0.000014	0.71159	
MZ_{14}-21	Banded ores	Sphalerite	0.09	0.313	0.833	0.714869	0.000015	0.71250	This paper
MZ_{14}-42	Veined ores	Sphalerite	0.075	1.01	0.215	0.712634	0.000011	0.71202	
MZ_{14}-60	Disseminated ores	Sphalerite	0.103	3.14	0.095	0.713121	0.000014	0.71285	

$(^{87}Sr/^{86}Sr)_t = {}^{87}Sr/^{86}Sr - {}^{87}Sr/^{87}Rb\ (e^{\lambda t} - 1)$, $\lambda_{Rb} = 1.41 \times 10^{-11}\ t^{-1}$, $t = 200$ Ma (Zhou et al., 2013a,b, 2015).

seawater has $\delta^{34}S$ values rang of +10 to +35‰ (Claypool et al., 1980; Sharp, 2017); H_2S in oil-gas reservoir has $\delta^{34}S$ values rang of +5 to +20‰ (Zhu et al., 2014); and gypsum-bearing evaporites within the regional sedimentary strata having $\delta^{34}S$ values of +22 to +28‰ (Zhou et al., 2013c,d).

Based on the bulk S isotopic data (Fig. 8a and b), Zhou et al. (2013c) suggested that the source of S is marine evaporites within the regional sedimentary strata. Compared with the above main S reservoirs, although both bulk (+8.8–+19.9‰) and *in situ* S isotopic data (+5.9–+20.7‰) are significantly higher than those of magma-derived S, they are similar to those of metamorphic rocks/fluids and marine-derived S (include H_2S reservoir gas, evaporites and connate seawater) (Fig. 8b and c). In addition, geological survey exhibited that Meso- to Neoproterozoic basements (low-grade metamorphic rocks) and Paleozoic sedimentary cover sequences (rich in gypsum and barite, $\delta^{34}S$ = +22–+28‰; late Ediacaran coeval seawater, $\delta^{34}S$ = +20–+35‰) are well-developed in the study region (Figs. 1 and 3) (Liu and Lin, 1999; Huang et al., 2004; Bai et al., 2013; Zhou et al., 2013d, 2018a; Liu et al., 2017a). Hence, metamorphic rocks/fluids and/or marine-derived S could be the source of S in the ore-forming fluids.

It has been well-documented that $\delta^{34}S_{barite} > \delta^{34}S_{fluid} > \delta^{34}S_{sulfide}$ if the hydrothermal minerals contain barite (Ohmoto, 1972; Ohmoto et al., 1990; Zhou et al., 2013c). Hence, the $\delta^{34}S_{fluid}$ value should be at least higher than the minimum or average $\delta^{34}S_{sulfide}$ value determined by *in situ* and bulk analyses (Fig. 8) as recorded by the paragenetic association of barite in post-ore phase (Fig. 4k and o; Zhou et al. 2013c), i.e. $\delta^{34}S_{fluid} > +5.9$ or +8.8‰ (minimum *in situ* and bulk $\delta^{34}S_{sulfide}$ values, respectively), and even +13.8‰ (mean value of all measured data). In addition, post-ore barite has a $\delta^{34}S$ value of +30.4‰ (Fig. 8b; Liu and Lin, 1999) that is higher than those of sulfides formed at main stage ($\delta^{34}S$ = +5.9–+20.7‰; Fig. 8b), which is due to the relatively oxidized environment at the post-ore stage (Liu, 2009; Zhou et al., 2013c) or mixing of another kind of fluid that was different from the fluid for Pb-Zn mineralization. The post-ore mineral assemblage shows that barite coexists with calcite (Fig. 4k and o), and the C—O isotopic compositions, and REE contents and patterns of post-ore calcite are similar to those of syn-ore calcite (Bao et al., 2013; Zhou et al., 2013c). This means that the fluid mixing should occur at syn-ore stage and there is no another fluid mixed at the post-ore stage. Hence, the $\delta^{34}S$ values of barite precipitated from the same ore-forming fluids should approximate to the total $\delta^{34}S$ values of the ore-forming fluids, i.e. $\delta^{34}S_{barite} \approx \delta^{34}S_{\Sigma S}$ (Ohmoto et al., 1990). This implies that the $\delta^{34}S_{fluid}$ value is similar to the $\delta^{34}S_{\Sigma S}$ value that is +30‰ or so. This rules out a single source of metamorphic rocks/fluids supplied the majority of S. On the other hand, other potential sources (H_2S reservoir gas, evaporites and coeval seawater) are related to marine sulfate, which have followed a variety of geochemical pathways that cause diverse isotope fractionation (Trudinger et al., 1985; Seal, 2006). Hence, given that reduced S is completely derived from gypsum-bearing evaporites, as thermochemical sulfide reduction (TSR) (see below) can generate up to +15‰ of $\Delta^{34}S_{sulfate\text{-}sulfide}$ value (Machel et al., 1995; Ohmoto and Goldhaber, 1997), so the theoretical $\delta^{34}S_{sulfide}$ values could change from +7‰ to +28‰, which can match with the observed *in situ* $\delta^{34}S$ values (+5.9–+20.7‰) (Fig. 7 and 8a-b) and S isotopic compositions of H_2S within oil-gas reservoir (Zhu et al., 2014). Similarly, if S is totally sourced from connate seawater, the theoretical $\delta^{34}S_{sulfide}$ values (+5–+35‰) generated by TSR can also match well with the determined *in situ* $\delta^{34}S$ values (+5.9–+20.7‰) (Figs. 7 and 8a–c) and S isotopic compositions of H_2S within oil-gas reservoir (Zhu et al., 2014). Therefore, integrated all the geological (Figs. 1–3) and geochemical (Figs. 7–12) evidence (see below), the most reasonable is that S in ore-forming fluids was derived from or flowed through multiple reservoirs (i.e. metamorphic rocks/fluids, gypsum-bearing evaporites, coeval seawater and H_2S reservoir gas).

5.1.2. Thermochemical or bacterial sulfate reduction?

It is well-known that the reduction of marine sulfate occurs either through abiotic thermochemical or bacterially mediated processes (Ohmoto et al., 1990; Machel et al., 1995; Hoefs, 2009). The process of thermochemical sulfate reaction (TSR), can produce sulfate-sulfide fractionations that range from 0‰ to as much as +15‰ (Worden et al., 1995; Ohmoto and Goldhaber, 1997; Zhu et al., 2014), whereas those associated with bacterial sulfate reduction (BSR) typically range from +15 to +60‰ (Goldhaber and Kaplan, 1975; Basuki et al., 2008). Moreover, both TSR and BSR are temperature-dependent. BSR has been documented at temperatures up to 110 °C (Jørgensen et al., 1992), but the optimum range is between 30 and 40 °C (Seal, 2006). In contrast, TSR occurs at temperatures > 100–140 °C and can produce abundant S^{2-} with relatively stable $\delta^{34}S$ values (Ohmoto et al., 1990; Machel et al., 1995). As the range of fluid inclusions homogenization temperatures (153–248 °C: Liu, 2009) is distinctly higher than that of bacteria survive, but which is benefit to TSR, so BSR played an insignificant role in the formation of S^{2-}. In addition, the Maozu deposit contains ~20 Mt of sulfide ore reserves, which need a large number of S^{2-} (Zhou et al., 2013c). Hence, TSR produced the majority of S^{2-} from SO_4^{2} in the Maozu deposit.

5.1.3. S isotope fractionation

As shown in Fig. 7, the sphalerite crystals have *in situ* $\delta^{34}S$ values (+15.9-+17.1‰) higher than those of paragenetic pyrite (+5.9–+11.2‰) (Fig. 7a and b) or lower than those of paragenetic pyrite (+19.2–+20.7‰) (Fig. 7d). In addition, previously reported bulk $\delta^{34}S$ values of pyrite, sphalerite and galena (Fig. 8a and b) also do not show the feature of $\delta^{34}S_{pyrite} > \delta^{34}S_{sphalerite} > \delta^{34}S_{galena}$ that would be expected for equilibrium fractionation of S isotopes (Ohmoto, 1972). Such S isotope signatures reflect that S isotopes in the mineralizing system occurred disequilibrium fractionation among precipitated sulfides, at least locally. Therefore, the $\delta^{34}S$ values of sulfides (especially pyrite) could not stand for the $\delta^{34}S_{fluids}$, as discussed above. In addition, previous studies suggested that the change of physical and chemical conditions (T, Eh, and pH, etc.), or insufficient time for isotope equilibrium can result in disequilibrium fractionation (Seal, 2006; Sharp, 2017). Furthermore, fluid mixing (see below) at early hydrothermal phase could cause the change of ore-forming environments in

Fig. 7. *In situ* $\delta^{34}S$ values in sphalerite and paragenetic pyrite.

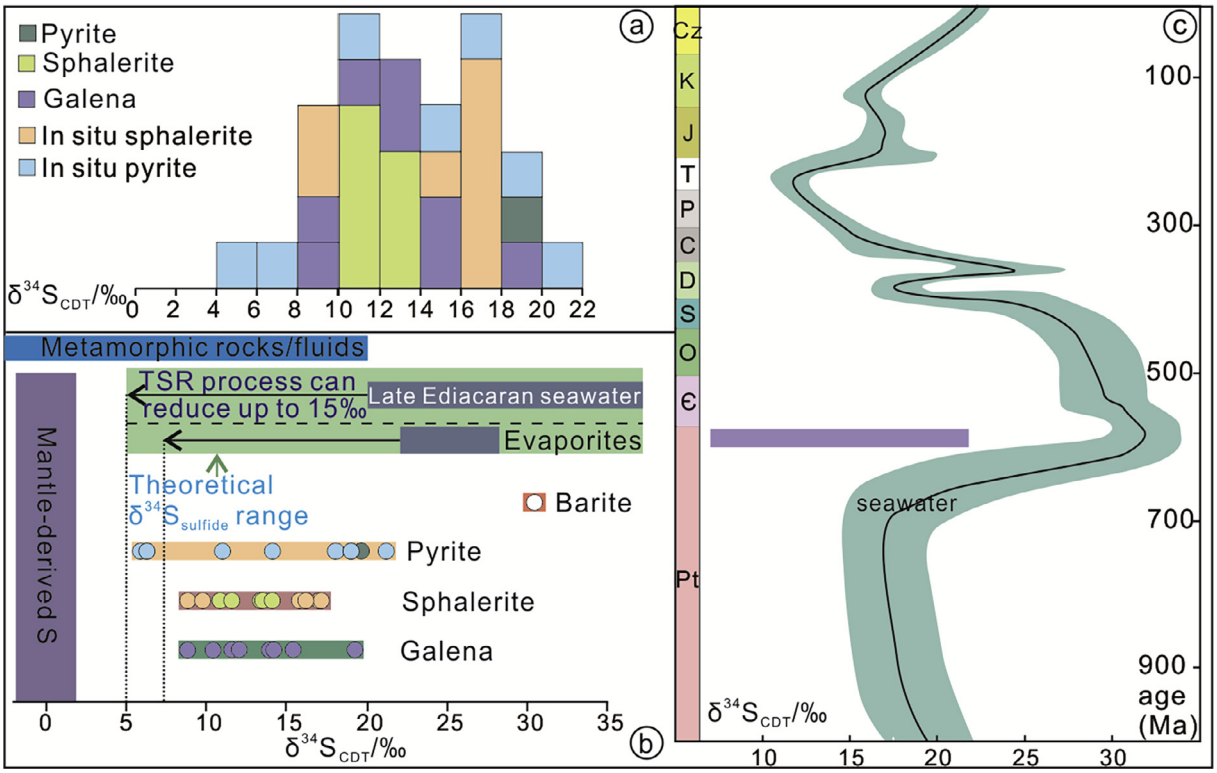

Fig. 8. a: Histogram of *in situ* and bulk S isotopic compositions (Liu and Lin, 1999; Liu, 2009; Zhou et al., 2013a); b: A comparison of $\delta^{34}S$ values between S-bearing minerals and metamorphic rocks/fluids (Ohmoto, 1986; Seal, 2006), mantle-derived S (Chaussidon et al., 1989), late Ediacaran seawater (Claypool et al., 1980), and evaporites (Huang et al., 2004; Zhou et al., 2013d); c: A comparison of S isotopes between sulfides and the evolution of seawater (Claypool et al., 1980).

hydrothermal systems and generate rapid precipitation of sulfides (Leach et al., 2005; Zhou et al., 2013a, 2014b). Hence, the variations of S isotopes during sulfide precipitation in the Maozu deposit (Figs. 7 and 8) was likely controlled by both dynamic and thermodynamics fractionations.

5.2. Sources of ore-forming metal

5.2.1. Implication from in situ Pb isotopes

The low U/Pb and Th/Pb ratios of galena suggest that the determined Pb isotopic ratios should approximate to the initial Pb isotopic compositions of mineralized fluids (Carr et al., 1995; Pass et al., 2014; Zhou et al., 2014b; Tan et al., 2017). Compared with the previous reported bulk Pb isotopic data (Table 2; Zhou et al., 2013c), the much narrower range of *in situ* Pb isotopic data (Figs. 9 and 10) suggests that *in situ* Pb isotopic data can truly reveal the source of Pb, because of bulk Pb isotopic data can be significantly affected by impurities enclosed by sulfides (such as diverse impurities in galena; Fig. 4c and h), and pollutants introduced by chemical analysis. This further indicates that Pb is derived from a single or well-mixed source (Fig. 9). In the plot of $^{207}Pb/^{204}Pb$ vs. $^{206}Pb/^{204}Pb$ (Fig. 9a), all the *in situ* Pb isotopic data plot above the Pb evolution curve of average upper crust, and fall into the field of modern lower crust, implying a clearly crustal source of Pb (Zartman and Doe, 1981). In addition, in the diagram of $^{208}Pb/^{204}Pb$ vs. $^{206}Pb/^{204}Pb$ (Fig. 9b), all the *in situ* Pb isotopic data fall into the overlapped field of modern lower crust and orogen, also indicating a crustal Pb source (Zartman and Doe, 1981).

Three potential metal source rocks have been identified in the study region, i.e. the Meso- to Neoproterozoic metamorphic rocks, Paleozoic sedimentary rocks, and the late Permian basalts of the ELIP (Zheng and Wang, 1991; Zhou et al., 2013b, 2018a; Bao et al., 2017; Tan et al., 2017). Compared with basements, sediments and basalts, at a given $^{206}Pb/^{204}Pb$ ratio (Fig. 9a), galena crystals display higher $^{207}Pb/^{204}Pb$ ratios than those of ore formation age-corrected basalts (~200 Ma: Zhou et al., 2013c). This rules out the possibility of basalts as a single source provided the majority of Pb. Furthermore, *in situ* Pb isotopic data fall into the overlapped field of age-corrected sediments and basements (Fig. 9a) (~200 Ma: Zhou et al., 2013c), revealing that both of them can singly supply the Pb. Therefore, integrated all the geological (Figs. 1–3) and geochemical (Figs. 7–11) evidence (see above and below), we interpret that Pb in the mineralizing fluids was mainly originated from and/or flowed through a mixed source of basements and sediments.

5.2.2. Implication from Rb-Sr isotopes

Due to no more suitable minerals and dating methods for base metal sulfide ore deposits, Rb-Sr dating of sphalerite is still the most reliable constraint on ore formation ages (Nakai et al., 1990; Brannon et al., 1992; Christensen et al., 1995; Li et al., 2005; Zhou et al., 2015). However, the real status of Rb and Sr in sphalerite is unclear and its Rb-Sr isotopic dating is very difficult. In this study, although we do not obtain the ideal sphalerite Rb-Sr isotopic age, Sr isotopes can be used to trace the sources and/or evolutions of ore-forming fluids (Yang and Zhou, 2001; Deng et al., 2015; Beaudoin and Chiaradia, 2016).

In order to use Sr isotopes of hydrothermal minerals for tracing, we need to know their initial $^{87}Sr/^{86}Sr$ ratios (Deng et al., 2000; Gromek et al., 2012; Zhou et al., 2013a). Syn-ore hydrothermal calcite Sm-Nd isochron dating yields an isotopic age of 196 ± 13 Ma (Zhou et al., 2013c), which is similar to the peaked ages (230–200 Ma) of Pb-Zn mineralization in the Upper Yangtze metallogenic province (Mao et al., 2012; Zhou et al., 2013a,c, 2015; Zhang et al., 2015). Hence, ~ 200 Ma was used to calculate the initial $^{87}Sr/^{86}Sr$ ratios of sphalerite separates and potential metal source rocks (i.e. basalts, sediments and basements) (Huang et al., 2004; Zhou et al., 2014b). All the sphalerite separates have $^{87}Sr/^{86}Sr_{200\ Ma}$ ratios ranging from 0.711 to 0.719, which are significantly higher than those of ore formation age-corrected basalts

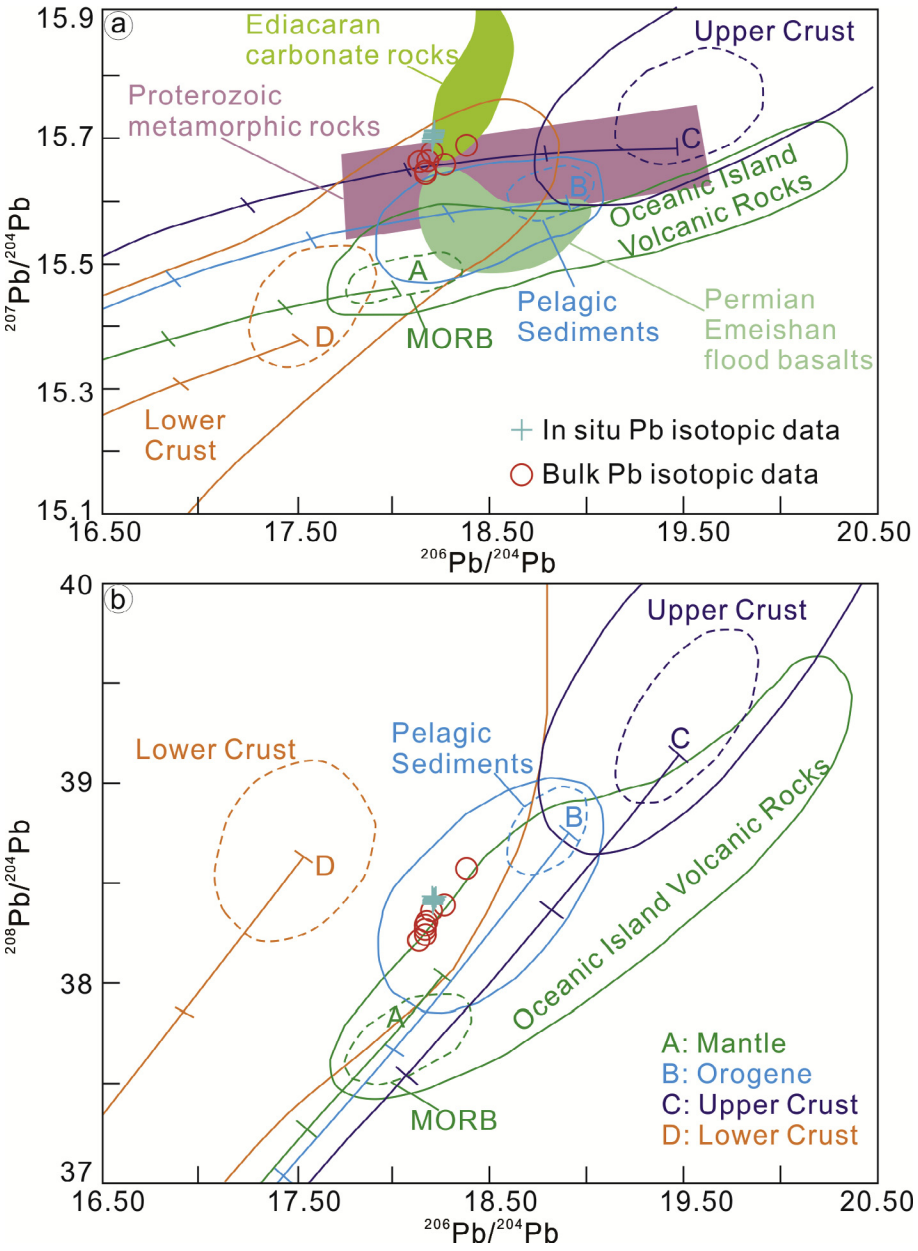

Fig. 9. Plots of $^{207}Pb/^{204}Pb$ vs. $^{206}Pb/^{204}Pb$ (a) and $^{208}Pb/^{204}Pb$ vs. $^{206}Pb/^{204}Pb$ (b). A brief comparison of the modern MORB, Pelagic sediment, Oceanic island volcanic rocks, Upper Crust and Lower Crust (Zartman and Doe, 1981), and whole-rock of basements, carbonates and basalts (age-corrected at 200 Ma; Huang et al., 2004; Li et al., 2007; Yan et al., 2007; Zhou et al., 2013b, 2014b); Solid lines enclose 80% of all data points for each field, and dashed lines enclose probable average values. Upper Crust (U), Orogen Belt (O), Mantle (M) and Lower Crust (L).

($^{87}Sr/^{86}Sr_{200\ Ma}$ = 0.704–0.708; Table 4; Fig. 11; Huang et al., 2004; and upper mantle: 0.704 ± 0.002; Faure, 1977), but are distinctly lower than those of age-corrected basements ($^{87}Sr/^{86}Sr_{200\ Ma}$ = 0.724–0.729; Table 4; Fig. 11; Li and Qin, 1988; Chen and Ran, 1992). On the other hand, sediments have $^{87}Sr/^{86}Sr_{200\ Ma}$ ratios ranging from 0.707 to 0.714 (Table 4; Fig. 11; Hu, 1999; Deng et al., 2000; Shi et al., 2003; Jiang and Li, 2005; Zhou et al., 2013b, 2014b, 2018a), which partly overlap with those of sphalerite separates (Fig. 11).

Neither basements, sediments nor basalts contain the Sr isotopic ratios that can match well with those of sphalerite separates (Fig. 11), implying that the ore-forming fluids were probably derived from or flowed through a mixed source. As our *in situ* S and Pb isotopic data rule out the possibility of basalts as a main source of mineralizing elements and associated fluids (Figs. 7–10), so such Sr isotope signatures of sphalerite separates indicate that the mineralizing fluids were most likely sourced from and/or flowed through basements and sediments, with a certain influence from basalts (Fig. 11). Furthermore, it is worth pointing out that among these sediments, early Cambrian black shales contain high radiogenic Sr isotopes with $^{87}Sr/^{86}Sr_{200\ Ma}$ ratios range of 0.712–0.714 (Table 4, Jiang and Li, 2005), which are much more similar to those of sphalerite separates. This means that black shales have played an important role in the formation of Zn-Pb sulfide ores in the Upper Yangtze province, i.e. they not only act as a key geochemical barrier, but also supply parts of ore-forming materials.

5.3. Ore formation process

The new evidence of *in situ* S-Pb and bulk Sr isotopic data (Figs. 7–11) suggests that the Maozu deposit has no significantly genetic relationship with Emeishan magmatism. However, we could not rule

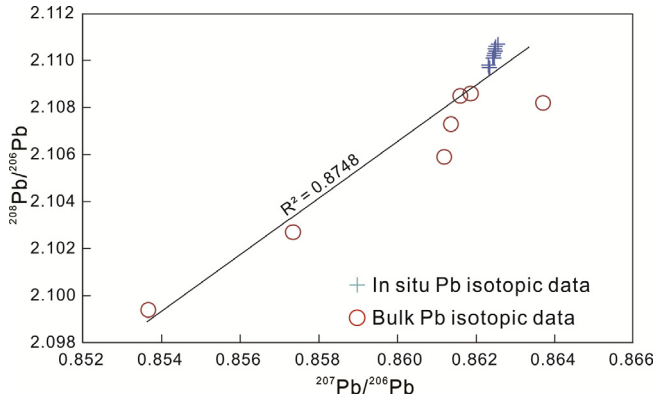

Fig. 10. Plot of $^{208}Pb/^{206}Pb$ vs. $^{207}Pb/^{206}Pb$. Bulk Pb isotopic data are from Zhou et al. (2013c).

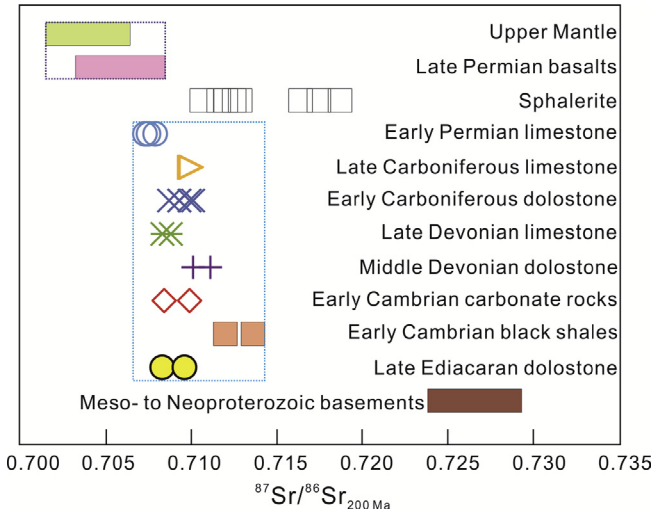

Fig. 11. A comparison of $^{87}Sr/^{86}Sr_{200\ Ma}$ ratios between sphalerite separates and potential metal source rocks (upper mantle, basalts, sediments and basements). Whole-rock Sr isotopic data are from Faure (1977), Cong (1988), Li and Qin (1988), Chen and Ran (1992); Hu (1999), Deng et al. (2000), Huang et al. (2004), Jiang and Li (2005), Shi et al. (2013) and Zhou et al. (2013a,b, 2014b, 2018a).

out the contribution from basalts completely through Pb and Sr isotopes (Figs. 9 and 11). In contrast, the spatially association between Pb-Zn ore bodies and basalts (Fig. 3b) suggests that the basalts maybe play a certain role in the formation of the Maozu deposit. Our previous studies suggested that the ELIP provided volatiles and elevated background geothermal gradient, and its basalts acted as an impermeable and protective layer (Zhou et al., 2018a,c). Hence, the formation of the Maozu deposit has indirect links with the ELIP, which are different from typical MVT deposits that have no spatial and temporal relationship with igneous activities (Leach et al., 2005). Moreover, the low-moderate temperatures (153–248 °C: Liu, 2009) and low salinities (2.8–5.3 wt% NaCl equiv.: He et al., 2006) of the Maozu deposit are also different from basin brines-related MVT deposits that have low temperatures (90–200 °C) and high salinities (10–30 wt% NaCl equiv.) (Leach et al., 2010). Furthermore, the ore-controlling reverse fault-fold tectonic systems (Fig. 3a and b) and high ore grades (> 10 wt% Pb + Zn), as well as abundant Cd, Ge and Ga, suggesting that the metallogenic characteristics of the Maozu deposit are really different from those of typical MVT deposits (Leach et al., 2005, 2010). Hence, integrated fluid compositions, geochronology and field data, the Maozu deposit was considered to be an epigenetic carbonate-hosted and fault-fold system-controlled deposit that formed during Early Mesozoic (196 Ma: Zhou et al., 2013c).

In summary, this paper proposes a comprehensive metallogenic model: a) During 263–259 Ma, the underplating and eruption of the basalts of the ELIP provided fluids and elevated background geothermal gradient, which facilitate and enhance the mobilization and extraction of ore-forming elements (e.g. Pb, Zn and Ag) from Proterozoic basements; b) Driven by the Indosinian Orogeny (257–200 Ma), the basement-derived fluids (as suggested by Pb-Sr isotopes, Figs. 9 and 11) migrated upward along several regional deep faults (such as Anninghe and Xiaojiang faults, Fig. 1b), and then released into secondary structures within Paleozoic sedimentary rocks (Figs. 1–3); and c) These metal rich fluids were trapped by the Maozu reverse fault-fold tectonic systems (Figs. 2 and 3) and mixed with multiple reservoirs S-bearing fluids (as indicated by S isotopes, Figs. 7 and 8). Such a fluid mixing process heated the sulfate-bearing fluids and then resulted in the formation of S^{2-} from SO_4^{2-} by TSR, and caused rapid sulfide precipitation at ~196 Ma (Zhou et al., 2013c). In addition, there is no another fluid mixed in the late phase indicates the post-ore minerals

Table 4
Sr isotopic ratios of whole-rock of sediments, basements, and basalts (and Upper Mantle) in the Upper Yangtze metallogenic province.

No.	Rock	$^{87}Rb/^{86}Sr$	$^{87}Sr/^{86}Sr$	$^{87}Sr/^{86}Sr_{200Ma}$	Reference
Late Permian Emeishan flood Basalts		0.7039–0.7078 (n = 85, mean 0.7058)			Huang et al. (2004)
D11	Early Permian limestone	0.001	0.7075	0.7075	Zhou et al. (2014b, 2018a)
D12	Early Permian limestone	0.001	0.7073	0.7073	
LMG-9	Early Permian limestone	0.001	0.7079	0.7079	Deng et al. (2000)
D8	Late Carboniferous limestone	0.007	0.7100	0.7100	Zhou et al. (2013a)
D9	Late Carboniferous limestone	0.020	0.7100	0.7099	
D35	Early Carboniferous dolostone	0.010	0.7101	0.7101	Zhou et al. (2014b)
D36	Early Carboniferous dolostone	0.001	0.7099	0.7099	
D13	Early Carboniferous dolostone	0.001	0.7093	0.7093	Hu (1999)
D14	Early Carboniferous dolostone	0.001	0.7087	0.7087	
D15	Early Carboniferous dolostone	0.006	0.7093	0.7093	
D6	Late Devonian limestone	0.0511	0.7085	0.7083	Zhou et al. (2013a)
D7	Late Devonian limestone	0.0003	0.7088	0.7088	
LMG-11	Middle Devonian dolostone	0.1325	0.7105	0.7101	Deng et al. (2000)
D3	Middle Devonian sandstone	0.7365	0.7132	0.7111	Zhou et al. (2013a)
Early Cambrian carbonate rocks		0.7084–0.7099 (n = 16, mean 0.7091)			Shi et al. (2013)
Early Cambrian black shales		0.7120–0.7136 (n = 2, mean 0.7128)			Jiang and Li (2005)
D1	Late Ediacaran dolostone	0.0019	0.7083	0.7083	Zhou et al. (2013a)
D2	Late Ediacaran dolostone	0.059	0.7098	0.7096	
Neo- to Mesoproterozoic metamorphic rocks		0.7243–0.7288 (n = 5, mean 0.7266)		Cong (1988), Li and Qin (1988), Chen and Ran (1992)	
Upper Mantle		0.704 ± 0.002			Faure (1977)

$(^{87}Sr/^{86}Sr)_t = {}^{87}Sr/^{86}Sr - {}^{87}Sr/^{87}Rb\ (e^{\lambda t} - 1)$, $\lambda_{Rb} = 1.41 \times 10^{-11}\, t^{-1}$, t = 200 Ma (Zhou et al., 2013a,b, 2015).

were precipitated from a relatively closed system. During the ore formation process, tectonic regime changed from compression to extension during Early Mesozoic facilitated the excretion of two kinds of ore-forming fluids, reverse fault-fold tectonic systems were beneficial to trap these fluids, black shales acted as geochemical barrier and provided parts of ore-forming elements, and the ELIP provided volatiles and its basalts acted as an impermeable and protective layer, all of which enabled the giant accumulation of Pb-Zn ores in the Upper Yangtze metallogenic province (Zhou et al., 2018a,b).

6. Conclusions

In situ S isotopic data indicate that S was derived from multiple reservoirs. TSR played a key role in the formation of S^{2-}. Both dynamic and thermodynamic fractionations jointly controlled the variations of S isotopes in sulfide minerals. *In situ* Pb and bulk Sr isotopic data imply that the ore-forming elements and associated fluids were mainly derived from a mixed source of basements and sediments, with a certain influence from the basalts of the ELIP. The change of tectonic regime from compression to extension during Early Mesozoic, the trap of reverse fault-fold tectonic systems, and the fluid mixing process played a crucial role in the formation of the carbonate-hosted epigenetic Zn-Pb deposits in the Upper Yangtze metallogenic province.

Acknowledgements

This research was financially supported by the National Key Research and Development Project of China (2017YFC0602502), the Key Project of National Natural Science Foundation of China (41430315), the National Basic Research Program of China (2014CB440905) and the National Natural Science Foundation of China (41763003). We thank Prof. Lin Ye (Institute of Geochemistry, CAS) for useful discussions and Prof. Franco Pirajno (Editor-in-Chief), Prof. Nuo Li (Associate Editor) and anonymous reviewers for their constructive suggestions and comments.

References

Anderson, G.M., 2008. The mixing hypothesis and the origin of Mississippi Valley-type ore deposits. Econ. Geol. 103, 1683–1690.
Bai, J., Huang, Z., Zhu, D., Yan, Z., Zhou, J., 2013. Isotopic compositions of sulfur in the Jinshachang lead-zinc deposit, Yunnan, China, and its implication on the formation of sulfur-bearing minerals. Acta Geol. Sin. 87, 1355–1369.
Bao, G.P., Cui, Y.L., Gao, J.G., 2013. REE geochemical features of hydrothermal calcite from Maozu Pb-Zn deposit, NE Yunnan Province, China. Acta Mineral. Sin. 33, 681–685 (in Chinese with English abstract).
Bao, Z., Li, Q., Wang, C.Y., 2017. Metal source of giant Huize Zn-Pb deposit in SW China: new constraints from in situ Pb isotopic compositions of galena. Ore Geol. Rev. 91, 824–836.
Bao, Z., Yuan, W., Yuan, H., Liu, X., Chen, K., Zong, C., 2016. Non-matrix-matched determination of lead isotope ratios in ancient bronze artifacts by femtosecond laser ablation multi-collector inductively coupled plasma mass spectrometry. Inter. J. Mass Spectrom. 402, 12–19.
Basuki, N.I., Taylor, B.E., Spooner, E.T.C., 2008. Sulfur isotope evidence for thermochemical reduction of dissolved sulfate in Mississippi valley type zinc-lead mineralization, Bongara area, northern Peru. Econ. Geol. 103, 183–799.
Beaudoin, G., Chiaradia, M., 2016. Fluid mixing in orogenic gold deposits: evidence from the H-O-Sr isotope composition of the Val-d'Or vein field (Abitibi, Canada). Chem. Geol. 437, 7–18.
Brannon, J.C., Podosek, F.A., McLimans, R.K., 1992. Alleghenian age of the Upper Mississippi Valley zinc-lead deposit determined by Rb-Sr dating of sphalerite. Nature 356, 509–511.
Carr, G.R., Dean, J.A., Suppel, D.W., Heithersay, P.S., 1995. Precise lead isotope fingerprinting of hydrothermal activity associated with Ordovician to Carboniferous metallogenic events in the Lachlan fold belt of New South Wales. Econ. Geol. 90, 1467–1505.
Chaussidon, M., Albarède, F., Sheppard, S.M.F., 1989. Sulphur isotope variations in the mantle from ion microprobe analyses of micro-sulphide inclusions. Earth Planet. Sci. Lett. 92, 144–156.
Chen, H.S., Ran, C.Y., 1992. In: Isotope Geochemistry of Copper Deposit in Kangdian Area. Geological Publishing House, Beijing, pp. 1–25 (in Chinese).
Chen, Q.L., 2002. Metallogenetic geological features and ore guides of high-grade Pb-Zn deposits in Yuhucun Formation, northeast Yunnan. Geol. Prospect. 38, 22–26 (in Chinese with English abstract).
Chi, G., Savard, M.M., 1997. Sources of basinal and Mississippi Valley-type mineralizing brines: mixing of evaporated seawater and halite-dissolution brine. Chem. Geol. 143, 121–125.
Christensen, J.N., Halliday, A.N., Vearncombe, J.R., Kesler, S.E., 1995. Testing models of large-scale crustal fluid flow using direct dating of sulfides Rb-Sr evidence for early dewatering and formation of Mississippi valley-type deposits, Canning Basin, Australia. Econ. Geol. 90, 877–884.
Claypool, G.E., Holser, W.T., Kaplan, I.R., Sakai, H., Zak, I., 1980. The age curves of sulfur and oxygen isotopes in marine sulfate and their mutual interpretation. Chem. Geol. 28, 199–260.
Cong, B.L., 1988. In: Evolution and Formation of Panxi Rift. Science Press, Beijing, pp. 10–33 (in Chinese).
Deloule, E., Allegre, C.J., Doe, B.R., 1986. Lead and sulfur isotope microstratigraphy in galena crystals from Mississippi Valley-type deposits. Econ. Geol. 81, 1307–1321.
Deng, H.L., Li, C.Y., Tu, G.Z., Zhou, Y.M., Wang, C.W., 2000. Strontium isotope geochemistry of the Lemachang independent silver ore deposit, northeastern Yunnan, China. Sci. China Earth Sci. 43, 337–346.
Deng, X.H., Chen, Y.J., Bagas, L., Zhou, H.Y., Yao, J.M., Zheng, Z., Wang, P., 2015. Isotope (S-Sr-Nd-Pb) constraints on the genesis of the ca. 850Ma Tumen Mo-F deposit in the Qinling Orogen, China. Precambr. Res. 266, 108–118.
Faure, G., 1977. Principles of Isotope Geology. John Wiley & Sons, New York, pp. 28–110.
Goldhaber, M.B., Kaplan, I.R., 1975. Controls and consequences of sulfate reduction rates in recent marine sediments. Soil Sci. 119, 42–55.
Gromek, P., Gleeson, S.A., Simonetti, A., 2012. A basement-interacted fluid in the N81 deposit, Pine Point Pb-Zn district, Canada: Sr isotopic analyses of single dolomite crystals. Mineral. Deposita 47, 749–754.
Guan, S.P., Li, Z.X., 1999. Pb and S isotope study of carbonate-hosted Pb-Zn deposits at the eastern margin of the Kangdian axis. Geol. Geochem. 27, 45–54 (in Chinese with English abstract).
Hauri, E.H., Papineau, D., Wang, J., Hillion, F., 2016. High-precision analysis of multiple sulfur isotopes using NanoSIMS. Chem. Geol. 420, 148–161.
He, S.H., Rong, H.F., Shang, W., Su, J.H., 2006. Geological characteristics and genesis of Maozu lead and zinc deposit. Yunnan. Mineral. Resour. Geol. 20, 397–402 (in Chinese with English abstract).
Hoefs, J., 2015. In: Stable Isotope Geochemistry, 7th ed. Springer-Verlag, Berlin Heidelberg. https://doi.org/10.1007/978-3-319-19716-6.
Hoefs, J., 2009. In: Stable Isotope Geochemistry, 6th ed. Springer-Verlag, Berlin Heidelberg. https://doi.org/10.1007/978-3-540-70708-0.
Hu, R., Fu, S., Huang, Y., Zhou, M., Fu, S., Zhao, C., Wang, Y., Bi, X., Xiao, J., 2017. The giant South China Mesozoic low-temperature metallogenic domain: reviews and a new geodynamic model. J. Asian Earth Sci. 137, 9–34.
Hu, R.Z., Zhou, M.F., 2012. Multiple Mesozoic mineralization events in South China-an introduction to the thematic issue. Mineral. Deposita 47, 579–588.
Hu, Y.G., 1999. (Ph.D. thesis) In: Ag Occurrence, Source of Ore-forming Metals and Mechanism of Yinchangpo Ag-Pb-Zn Deposit, Guizhou. Institute of Geochemistry, Chinese Academy of Sciences, pp. 10–55 (in Chinese with English abstract).
Huang, Z.L., Chen, J., Han, R.S., Li, W.B., Liu, C.Q., Zhang, Z.L., Ma, D.Y., Gao, D.R., Yang, H.L., 2004. In: Geochemistry and Ore-formation of the Huize Giant Lead-zinc Deposit, Yunnan, Province, China-Discussion on the Relationship Between Emeishan Flood Basalts and Lead-zinc Mineralization. Geological Publishing House, Beijing, pp. 1–204 (in Chinese).
Huang, Z., Li, X., Zhou, M., Li, W., Jin, Z., 2010. REE and C-O isotopic geochemistry of calcites from the word-class Huize Pb-Zn deposits, Yunnan, China: Implication for the ore genesis. Acta Geol. Sin. 84, 597–613.
Ikehata, K., Notsu, K., Hirata, T., 2008. In situ determination of Cu isotope ratios in copper-rich materials by NIR femtosecond LA-MC-ICP-MS. J. Anal. Atom. Spectrom. 23, 1003–1008.
Jian, P., Li, D.Y., Kröner, A., Zhang, Q., Wang, Y.Z., Sun, X.M., Zhang, W., 2009. Devonian to Permian plate tectonic cycle of the Paleo-Tethys Orogen in southwest China (II): insights from zircon ages of ophiolites, arc/back-arc assemblages and within-plate igneous rocks and generation of the Emeishan CFB province. Lithos 113, 767–784.
Jiang, Y.H., Li, S.R., 2005. Study on the isotope data tracing and isotopic chronology in the black-rock series type Ni-Mo deposit in the Lower Cambrian in Hunan and Guizhou provinces. J. Mineral. Petrol. 25, 62–66 (in Chinese with English abstract).
Jin, C.H., Jiang, S.P., Qi, C.L., Zhang, X.G., Zhang, Y., Shen, Z.W., Zhang, D., 2015. Ore-controlling factors and ore prospecting direction of the Maozu deposit. Mineral. Resour. Geol. 29, 1–6 (in Chinese with English abstract).
Jin, Z.G., Zhou, J.X., Huang, Z.L., Ye, L., Luo, K., Gao, J.G., Chen, X.L., Wang, B., Peng, S., 2016. Ore genesis of the Nayongzhi Pb-Zn deposit, Puding city, Guizhou Province, China: evidences from S and in situ Pb isotopes. Acta Petrol. Sin. 32, 3441–3455 (in Chinese with English abstract).
Jones, H.D., Kesler, S.E., Furman, F.C., Kyle, J.R., 1996. Sulfur isotope geochemistry of southern Appalachian Mississippi Valley-type deposits. Econ. Geol. 91, 355–367.
Jørgenson, B.B., Isaksen, M.F., Jannasch, H.W., 1992. Bacterial sulfate reduction above 100 °C in deep sea hydrothermal vent sediments. Science 258, 1756–1757.
Kesler, S.E., Cumming, G.L., Krstic, D., Appold, M.S., 1994. Lead isotope geochemistry of Mississippi Valley-type deposits of the southern Appalachians. Econ. Geol. 89, 307–321.
LaFlamme, C., Martin, L., Jeon, H., Reddy, S.M., Selvaraja, V., Caruso, S., Bui, T.H., Roberts, M.P., Voute, F., Hagemann, S., Wacey, D., 2016. In situ multiple sulfur isotope analysis by SIMS of pyrite, chalcopyrite, pyrrhotite, and pentlandite to refine magmatic ore genetic models. Chem. Geol. 444, 1–15.
Leach, D.L., Bradley, D.C., Huston, D., Pisarevsky, S.A., Taylor, R.D., Gardoll, S.J., 2010. Sediment-hosted lead-zinc deposits in earth history. Econ. Geol. 105, 593–625.
Leach, D.L., Sangster, D., Kelley, K.D., Large, R.R., Garven, G., Allen, C., Gutzmer, J., Walters, S., 2005. Sediment-hosted lead-zinc deposits: a global perspective. Econ.

Geol. 100th Anniversary Volume, 561–607.
Li, B., Zhou, J., Li, Y., Chen, A., Wang, R., 2016. Geology and isotope geochemistry of the Yinchanggou-Qiluogou Pb-Zn deposit, Sichuan province, Southwest China. Acta Geol. Sin Engl. Ed. 90, 1768–1779.
Li, B., Zhou, J.X., Huang, Z.L., Yan, Z.F., Bao, G.P., Sun, H.R., 2015. Geological, rare earth elemental and isotopic constraints on the origin of the Banbanqiao Zn–Pb deposit, southwest China. J. Asian Earth Sci. 111, 100–112.
Li, F.H., Qin, J.M., 1988. In: Presinian System in Kangdian Area. Chongqing Press, Chongqing, pp. 15–45 (in Chinese).
Li, H., Zhang, Z., Santosh, M., Lv, L., Han, L., Liu, W., 2017. Late Permian basalts in the Yanghe area, eastern Sichuan Province, SW China: implications for the geodynamic of the Emeishan flood basalts province and Permian global mass extinction. J. Asian Earth Sci. 134, 293–308.
Li, Q.L., Chen, F.K., Wang, X.L., Li, C.F., 2005. Ultra-low procedural blank and the single grain mica Rb–Sr isochron dating. Chin. Sci. Bull. 50, 2861–2865.
Li, Q.L., Li, X.H., Liu, Y., Wu, F.Y., Yang, J.H., Mitchell, R.H., 2010. Precise U-Pb and Th–Pb age determination of kimberlitic perovskites by secondary ion mass spectrometry. Chem. Geol. 269, 396–405.
Li, W.B., Huang, Z.L., Yin, M.D., 2007. Dating of the giant Huize Zn-Pb ore field of Yunnan province, southwest China: constraints from the Sm-Nd system in hydrothermal calcite. Resour. Geol. 57, 90–97.
Lin, Z.Y., Wang, D.H., Zhang, C.Q., 2010. Rb-Sr isotopic age of sphalerite from the Paoma lead-zinc deposit in Sichuan Province and its implications. Geol. China 37, 488–496 (in Chinese with English abstract).
Liu, H.C., Lin, W.D., 1999. In: Study on the Law of Pb-Zn-Ag Ore Deposit in Northeast Yunnan, China. Yunnan University Press, Kunming, pp. 1–468 (in Chinese).
Liu, X., Liang, Q., Li, Z., Castillo, P.R., Shi, Y., Xu, J., Huang, X., Liao, S., Huang, W., Wu, W., 2017a. Origin of Permian extremely high Ti/Y mafic lavas and dykes from western Guangxi, SW China: implications for the Emeishan mantle plume magmatism. J. Asian Earth Sci. 141, 97–111.
Liu, W.H., Zhang, J., Wang, J., 2017b. Sulfur isotope analysis of carbonate-hosted Zn–Pb deposits in northwestern Guizhou Province, Southwest China: implications for the source of reduced sulfur. J. Geochem. Explor. 181, 31–44.
Liu, W.Z., 2009. Geological and geochemical characteristics and metallogenic mechanism analysis of the Pb-Zn deposit in Maozu, Yunnan, China. J. Chengdu Uni. Technol. (Sci. Technol. Ed.) 36, 480–486.
Machel, H.G., Krouse, H.R., Sassen, R., 1995. Products and distinguishing criteria of bacterial and thermo-chemical sulfate reduction. Appl. Geochem. 10, 373–389.
Mao, J.W., Zhou, Z.H., Feng, C.Y., Wang, Y.T., Zhang, C.Q., Peng, H.J., Miao, Y., 2012. A preliminary study of the Triassic large-scale mineralization in China and its geodynamic setting. Geol. China 39, 1437–1471 (in Chinese with English abstract).
Muchez, P., Heijlen, W., Banks, D., Blundell, D., Boni, M., Grandia, F., 2005. Extensional tectonics and the timing and formation of basin-hosted deposits in Europe. Ore Geol. Rev. 27, 241–267.
Nakai, S.I., Halliday, A.N., Kesler, S.E., Jones, H.D., 1990. Rb-Sr dating of sphalerites from Tennessee and the genesis of Mississippi Valley type ore-deposits. Nature 346, 354–357.
Ohmoto, H., 1972. Systematics of sulfur and carbon isotopes in hydrothermal ore deposits. Econ. Geol. 67, 551–579.
Ohmoto, H., 1986. Stable isotope geochemistry of ore deposits. Rev. Mineral. 16, 185–225.
Ohmoto, H., Goldhaber, M.B., 1997. Sulfur and carbon isotopes. In: Barnes, H.L. (Ed.), Geochemistry of Hydrothermal Ore Deposits, third ed. Wiley, New York, pp. 517–611.
Ohmoto, H., Kaiser, C.J., Geer, K.A., 1990. Systematic of sulfur isotopes in recent marine sediments and ancient sediment–hosted base metal deposits. In: Herbert, H.K., Ho, S.E. (Eds.), Stable Isotopes and Fluid Processes in Mineralization. Geol. Dep. Univ. Extens. Univ., Western Australia, pp. 70–120.
Pass, H.E., Cookem, D.R., Davidson, G., Maas, R., Dipple, G., Rees, C., Ferreira, L., Taylor, C., Deyell, C.L., 2014. Isotope geochemistry of the northeast zone, Mount Polley alkalic Cu-Au-Ag porphyry deposit, British Columbia: a case for carbonate assimilation. Econ. Geol. 109, 859–890.
Paul, B., Woodhead, J.D., Hergt, J., Danyushevsky, L., Kunihiro, T., Nakamura, E., 2011. Melt inclusion Pb-isotope analysis by LA–MC-ICPMS: assessment of analytical performance and application to OIB genesis. Chem. Geol. 289, 210–223.
Peevler, J., Fayek, M., Misra, K.C., Riciputi, L.R., 2003. Sulfur isotope microanalysis of sphalerite by SIMS: constraints on the genesis of Mississippi valley-type mineralization, from the Mascot-Jefferson City district, East Tennessee. J. Geochem. Explor. 80, 277–296.
Qiu, L., Tang, S.L., Wang, Q., Yang, W.X., Tang, X.L., Wang, J.B., 2016. Mesozoic geology of southwestern China: Indosinian foreland overthrusting and subsequent deformation. J. Asian Earth Sci. 122, 91–105.
Reid, A., Wilson, C.J., Shun, L., Pearson, N., Belousova, E., 2007. Mesozoic plutons of the Yidun Arc, SW China: U/Pb geochronology and Hf isotopic signature. Ore Geol. Rev. 31, 88–106.
Resano, M., Aramendía, M., Rello, L., Calvo, M.L., Bérail, S., Pécheyran, C., 2013. Direct determination of Cu isotope ratios in dried urine spots by means of fs-LA-MC-ICPMS. Potential to diagnose Wilson's disease. J. Analytical Atomic Spectrom. 28, 98–106.
Ripley, E.M., Li, C., Moore, C.H., Schmitt, A.K., 2010. Micro-scale S isotope studies of the Kharaelakh intrusion, Noril'sk region, Siberia: constraints on the genesis of coexisting anhydrite and sulfide minerals. Geochim. Cosmochim. Acta 74, 634–644.
Rye, R.O., 2005. A review of the stable-isotope geochemistry of sulfate minerals in selected igneous environments and related hydrothermal systems. Chem. Geol. 215, 5–36.
Schmitt, A.K., Chamberlain, K.R., Swapp, S.M., Harrison, T.M., 2010. In situ U-Pb dating of micro-baddeleyite by secondary ion mass spectrometry. Chem. Geol. 269, 386–395.
Seal, I.R., 2006. Sulfur isotope geochemistry of sulfide minerals. Rev. Mineral. Geochem. 61, 633–677.
Seal, R.R., Alpers, C.N., Rye, R.O., 2000. Stable isotope systematics of sulfate minerals. Rev. Mineral. Geochem. 40, 541–602.
Sharp, Z., 2017. Principles of Stable Isotope Geochemistry 2nd ed. doi: 10.5072/FK2GB24S9F.
Shi, H., Huang, S.J., Shen, L.C., Zhang, M., 2003. Strontium isotope composition of the Cambrian Luojiaguo section in Xiushan, Chongqing and its stratigraphic significance. J. Stratigraphy 27, 71–76 (in Chinese with English abstract).
Souders, A.K., Sylvester, P.J., 2010. Accuracy and precision of non-matrix-matched calibration for lead isotope ratio measurements of lead-poor minerals by LA-MC-ICPMS. J. Anal. Atom. Spectrom. 25, 975–988.
Steinhoefel, G., Horn, I., von Blanckenburg, F., 2009. Micro-scale tracing of Fe and Si isotope signatures in banded iron formation using femtosecond laser ablation. Geochim. Cosmochim. Acta 73, 5343–5360.
Sun, H.R., Zhou, J.X., Huang, Z.L., Fan, H.F., Ye, L., Luo, K., Gao, J.G., 2016. The genetic relationship between Cu-and Zn-dominant mineralization in the Tianbaoshan deposit. Southwest China. Acta Petrol. Sin. 32, 3407–3417.
Tan, S.C., Zhou, J.X., Li, B., Zhao, J.X., 2017. In situ Pb and bulk Sr isotope analysis of the Yinchanggou Pb-Zn deposit in Sichuan Province (SW China): constraints on the origin and evolution of hydrothermal fluids. Ore Geol. Rev. 91, 432–443.
Tang, Y.Y., Bi, X.W., Fayek, M., Hu, R.Z., Wu, L.Y., Zou, Z.C., Feng, C.X., Wang, X.S., 2014. Microscale sulfur isotopic compositions of sulfide minerals from the Jinding Zn-Pb deposit, Yunnan Province, Southwest China. Gondwana Res. 26, 594–607.
Trudinger, P.A., Chambers, L.A., Smith, J.W., 1985. Low-temperature sulphate reduction: biological versus abiological. Can. J. Earth Sci. 22, 1910–1918.
Wang, C.M., Deng, J., Carranza, E.J.M., Lei, X.R., 2014. Nature, diversity and temporal-spatial distributions of sediment-hosted Pb-Zn deposit in China. Ore Geol. Rev. 56, 327–351.
Wang, C.Y., Wei, B., Zhou, M.F., Minh, D.H., Qi, L., 2018. A synthesis of magmatic Ni-Cu-(PGE) sulfide deposits in the ~260 Ma Emeishan large igneous province, SW China and Northern Vietnam. J. Asian Earth Sci. 154, 162–186.
Wei, A.Y., Xue, C.D., Xiang, K., Li, J., Liao, C., Akhter, Q.J., 2015. The ore-forming process of the Maoping Pb-Zn deposit, northeastern Yunnan, China: constraints from cathodoluminescence (CL) petrography of hydrothermal dolomite. Ore Geol. Rev. 70, 562–577.
Worden, R.H., Smalley, P.C., Oxtoby, N.H., 1995. Gas souring by the thermo chemical sulfate reduction at 140 °C. AAPG Bull. 79, 854–863.
Xu, Y., Huang, Z., Zhu, D., Luo, T., 2014. Origin of hydrothermal deposits related to the Emeishan magmatism. Ore Geol. Rev. 63, 1–8.
Yan, Z.F., Huang, Z.L., Xu, C., Chen, M., Zhang, Z.L., 2007. Signatures of the source for the Emeishan flood basalts in the Ertan area: Pb isotope evidence. Chin. J. Geochem. 26, 207–213.
Yang, J.H., Zhou, X.H., 2001. Rb-Sr, Sm-Nd, and Pb isotope systematics of pyrite: implications for the age and genesis of lode gold deposits. Geology 29, 711–714.
Yuan, H.L., Yin, C., Liu, X., Chen, K.Y., Bao, Z.A., Zong, C.L., Dai, M.N., Lai, S.C., Wang, R., Jiang, S.Y., 2015. High precision *in-situ* Pb isotopic analysis of sulfide minerals by femtosecond laser ablation multi-collector inductively coupled plasma mass spectrometry. Sci. China Earth Sci. 58, 1713–1721.
Zartman, R.E., Doe, B.R., 1981. Plumbotectonics-the model. Tectonophysics 75, 135–162.
Zhang, C., Wu, Y., Hou, L., Mao, J., 2015. Geodynamic setting of mineralization of Mississippi Valley-type deposits in world-class Sichuan-Yunnan-Guizhou Zn-Pb triangle, southwest China: implications from age-dating studies in the past decade and the Sm-Nd age of the Jinshachang deposit. J. Asian Earth Sci. 103, 103–114.
Zhang, J., Lin, Y., Yang, W., Shen, W., Hao, J., Hu, S., Cao, M., 2014. Improved precision and spatial resolution of sulfur isotope analysis using NanoSIMS. J. Anal. Atom. Spectrom. 29, 1934–1943.
Zheng, M.H., Wang, X.C., 1991. Genesis of the Daliangzi Pb-Zn deposit in Sichuan, China. Econ. Geol. 86, 831–846.
Zheng, R.H., Gao, J.G., Nian, H.L., Jia, F.J., 2015. Rb-Sr isotopic compositions of sphalerite and its geological implications for Maozu Pb-Zn deposit, northeast Yunnan Province, China. Acta Mineral. Sin. 35, 435–438 (in Chinese with English abstract).
Zhou, C.X., Wei, C.S., Guo, J.Y., 2001. The source of metals in the Qilingchang Pb-Zn deposit, Northeastern Yunnan, China: Pb-Sr isotope constraints. Econ. Geol. 96, 583–598.
Zhou, J., Huang, Z., Bao, G., Gao, J., 2013a. Sources and thermo-chemical sulfate reduction for reduced sulfur in the hydrothermal fluids, southeastern SYG Pb-Zn metallogenic province, SW China. J. Earth Sci. 24, 759–771.
Zhou, J., Huang, Z., Yan, Z., 2013b. The origin of the Maozu carbonate-hosted Pb-Zn deposit, southwest China: constrained by C-O-S-Pb isotopic compositions and Sm-Nd isotopic age. J. Asian Earth Sci. 73, 39–47.
Zhou, J.X., Gao, J.G., Chen, D., Liu, X.K., 2013c. Ore genesis of the Tianbaoshan carbonate-hosted Pb–Zn deposit, Southwest China: geologic and isotopic (C-H-O-S-Pb) evidence. Inter. Geol. Rev. 55, 1300–1310.
Zhou, J., Huang, Z., Zhou, M., Li, X., Jin, Z., 2013d. Constraints of C-O-S-Pb isotope compositions and Rb-Sr isotopic age on the origin of the Tianqiao carbonate-hosted Pb-Zn deposit, SW China. Ore Geol. Rev. 53, 77–92.
Zhou, J.X., Bai, J.H., Huang, Z.L., Zhu, D., Yan, Z.F., Lv, Z.C., 2015. Geology, isotope geochemistry and geochronology of the Jinshachang carbonate-hosted Pb-Zn deposit, southwest China. J. Asian Earth Sci. 98, 272–284.
Zhou, J.X., Huang, Z.L., Lv, Z.C., Zhu, X.K., Gao, J.G., Mirnejad, H., 2014a. Geology, isotope geochemistry and ore genesis of the Shanshulin carbonate-hosted Pb-Zn deposit, southwest China. Ore Geol. Rev. 63, 209–225.
Zhou, J.X., Huang, Z.L., Zhou, M.F., Zhu, X.K., Muchez, P., 2014b. Zinc, sulfur and lead isotopic variations in carbonate-hosted Pb-Zn sulfide deposits, southwest China. Ore

Geol. Rev. 58, 41–54.
Zhou, J.X., Luo, K., Li, B., Huang, Z.L., Yan, Z.F., 2016a. Geological and isotopic constraints on the origin of the Anle carbonate-hosted Zn-Pb deposit in northwestern Yunnan Province, SW China. Ore Geol. Rev. 74, 88–100.
Zhou, J.X., Dou, S., Huang, Z.L., Cui, Y.L., Ye, L., Li, B., Gan, T., Sun, H.R., 2016b. Origin of the Luping Pb deposit in the Beiya area, Yunnan Province, SW China: constraints from geology, isotope geochemistry and geochronology. Ore Geol. Rev. 72, 179–190.
Zhou, J.X., Xiang, Z.Z., Zhou, M.F., Feng, Y.X., Luo, K., Huang, Z.L., Wu, T., 2018a. The giant Upper Yangtze Pb-Zn province in SW China: reviews, new advances and a new genetic model. J. Asian Earth Sci. 154, 280–315.
Zhou, J.X., Wang, X.C., Wilde, S.A., Luo, K., Huang, Z.L., Wu, T., Jin, Z.G., 2018b. New insights into the metallogeny of MVT Pb-Zn deposits: A case study from the Nayongzhi in South China, using field data, fluid compositions, and in situ S-Pb isotopes. Am. Mineral. 103, 91–108.
Zhou, J.X., Luo, K., Wang, X.C., Wilde, S.A., Wu, T., Huang, Z.L., Cui, Y.L., Zhao, J.X., 2018c. Ore genesis of the Fule Pb-Zn deposit and its relationship with the Emeishan Large Igneous Province: evidence from mineralogy, bulk C-O-S and in situ S-Pb isotopes. Gondwana Res. 54, 161–179.
Zhou, M.F., Yan, D.P., Kennedy, A.K., Li, Y.Q., Ding, J., 2002. SHRIMP zircon geochronological and geochemical evidence for Neo-Proterozoic arc-related magmatism along the western margin of the Yangtze Block, South China. Earth Planet. Sci. Lett. 196, 1–67.
Zhou, M.F., Zhao, X.F., Chen, W.T., Li, X.C., Wang, W., Yan, D.Y., Qiu, H.N., 2014c. Proterozoic Fe-Cu metallogeny and supercontinental cycles of the southwestern Yangtze Block, southern China and northern Vietnam. Earth Sci. Rev. 139, 59–82.
Zhu, C., Wen, H., Zhang, Y., Fan, H., 2016. Cadmium and sulfur isotopic compositions of the Tianbaoshan Zn-Pb-Cd deposit, Sichuan Province, China. Ore Geol. Rev. 76, 152–162.
Zhu, G.Y., Fei, A.G., Zhao, J., Liu, C., 2014. Sulfur isotopic fractionation and mechanism for thermochemical sulfate reduction genetic H_2S. Acta Petrol. Sin. 30 3772–2786.